Liprin-α3 controls vesicle docking and exocytosis at the active zone of hippocampal synapses

Man Yan Wong[a], Changliang Liu[a], Shan Shan H. Wang[a], Aram C. F. Roquas[a,1], Stephen C. Fowler[b], and Pascal S. Kaeser[a,2]

[a]Department of Neurobiology, Harvard Medical School, Boston, MA 02115; and [b]Department of Pharmacology and Toxicology, University of Kansas, Lawrence, KS 66045

Edited by Thomas C. Südhof, Stanford University School of Medicine, Stanford, CA, and approved January 9, 2018 (received for review November 1, 2017)

The presynaptic active zone provides sites for vesicle docking and release at central nervous synapses and is essential for speed and accuracy of synaptic transmission. Liprin-α binds to several active zone proteins, and loss-of-function studies in invertebrates established important roles for Liprin-α in neurodevelopment and active zone assembly. However, Liprin-α localization and functions in vertebrates have remained unclear. We used stimulated emission depletion superresolution microscopy to systematically determine the localization of Liprin-α2 and Liprin-α3, the two predominant Liprin-α proteins in the vertebrate brain, relative to other active-zone proteins. Both proteins were widely distributed in hippocampal nerve terminals, and Liprin-α3, but not Liprin-α2, had a prominent component that colocalized with the active-zone proteins Bassoon, RIM, Munc13, RIM-BP, and ELKS. To assess Liprin-α3 functions, we generated Liprin-α3–KO mice by using CRISPR/Cas9 gene editing. We found reduced synaptic vesicle tethering and docking in hippocampal neurons of Liprin-α3–KO mice, and synaptic vesicle exocytosis was impaired. Liprin-α3 KO also led to mild alterations in active zone structure, accompanied by translocation of Liprin-α2 to active zones. These findings establish important roles for Liprin-α3 in active-zone assembly and function, and suggest that interplay between various Liprin-α proteins controls their active-zone localization.

Liprin-α | active zone | synaptic vesicle exocytosis | vesicle docking | active zone assembly

Exocytosis of synaptic vesicles in a nerve terminal is mediated by specialized sites called active zones. Active zones provide slots for synaptic vesicle docking and priming, tether Ca^{2+} channels, and target fusion to membrane domains opposed to postsynaptic receptors (1). At vertebrate synapses, active zones are thought to be composed of six protein families: RIM, ELKS, Munc13, RIM-BP, Piccolo/Bassoon, and Liprin-α (Fig. 1*A*). Many additional proteins that are not restricted to the active zone, including cytoskeletal proteins, SNAREs, Ca^{2+} channels, and cell adhesion proteins, are also present.

Although mouse genetic experiments have led to insights into functions of most vertebrate active-zone proteins, such experiments have not been pursued for Liprin-α. Liprin-α was identified through the binding to the phosphotyrosine phosphatase LAR (2) and was hypothesized to be a vertebrate active-zone protein based on biochemical interactions with RIM and ELKS (3, 4). Invertebrate data support broad presynaptic functions for Liprin-α. At the *Caenorhabditis elegans* neuromuscular junction, deletion of the Liprin-α homolog syd-2 alters active-zone structure and disrupts synaptic vesicle accumulation in nerve terminals (5–7). The fly homolog Dliprin-α regulates presynaptic morphogenesis of the neuromuscular junction and is required for target selection in the retina (8–10). These effects are consistent with the many biochemical activities of Liprin-α. In addition to interacting with LAR, RIM, and ELKS (2–4), Liprin-α binds to itself and β-liprins, GIT, CASK, RSY-1, mDiaphenous, and KIF1A (1, 2, 7, 11, 12). These interactions predict broad cellular functions.

Vertebrates express four genes, *Ppfia1–Ppfia4*, encoding Liprin-α1–Liprin-α4. Liprin-α1 is expressed within and outside the nervous system, and, like Liprin-α4, brain expression is low and restricted to a few areas. In contrast, Liprin-α2 and Liprin-α3 are strongly and specifically expressed in the brain (2, 13–15). Their subcellular localization and function, however, remained uncertain. Confocal microscopy partially supported synaptic localization of Liprin-α2 and Liprin-α3 (14, 15), and postsynaptic localization was favored by immunogold labeling experiments with Liprin-α2 antibodies (16). A recent study, however, found that knockdown of Liprin-α2 impaired synaptic transmission, and effects were more consistent with presynaptic than with postsynaptic roles (17).

Here, we set out to determine localization and function of Liprin-α in the brain. We found that Liprin-α3 and Liprin-α2 are widely distributed in hippocampal nerve terminals. In addition, Liprin-α3, but not Liprin-α2, had a prominent component that strongly colocalized with active-zone proteins. Liprin-α3–KO mice, which we generated for this study, displayed impairments in synaptic vesicle docking, tethering, and exocytosis, establishing presynaptic roles for Liprin-α3 in synaptic transmission.

Results

Localization of Liprin-α and Active-Zone Proteins Using Stimulated Emission Depletion Microscopy. We set out to evaluate Liprin-α2 and Liprin-α3 localization at hippocampal synapses. Similar to the approach used at the fly neuromuscular junction (18), we performed stimulated emission depletion (STED) superresolution microscopy because diffraction-limited microscopy is not sufficient to determine whether a protein is localized to the active zone, to synaptic vesicles inside a nerve terminal, or to the postsynaptic

Significance

The presynaptic active zone is important for precise and fast information transfer at central nervous synapses. Invertebrate studies have indicated that Liprin-α proteins are important for active zone assembly and function, but localization and function of vertebrate Liprin-α proteins have remained enigmatic, and pre- or postsynaptic localization and roles have been proposed. Here we used stimulated emission depletion microscopy to directly show that Liprin-α3, but not Liprin-α2, prominently localizes to the active zone. We then generated Liprin-α3–KO mice and found that active zone structure and synaptic vesicle docking and exocytosis are impaired at their synapses. These data establish important functions of Liprin-α3 at the active zone of vertebrate synapses.

Author contributions: M.Y.W. and P.S.K. designed research; M.Y.W., C.L., S.S.H.W., and A.C.F.R. performed research; M.Y.W., C.L., and S.C.F. contributed new reagents/analytic tools; M.Y.W., C.L., S.S.H.W., A.C.F.R., and P.S.K. analyzed data; and M.Y.W., C.L., and P.S.K. wrote the paper.

The authors declare no conflict of interest.

This article is a PNAS Direct Submission.

[1]Present address: Vrije Universiteit Amsterdam, 1081 HV Amsterdam, The Netherlands.

[2]To whom correspondence should be addressed. Email: kaeser@hms.harvard.edu.

This article contains supporting information online at www.pnas.org/lookup/suppl/doi:10.1073/pnas.1719012115/-/DCSupplemental.

Published online February 8, 2018.

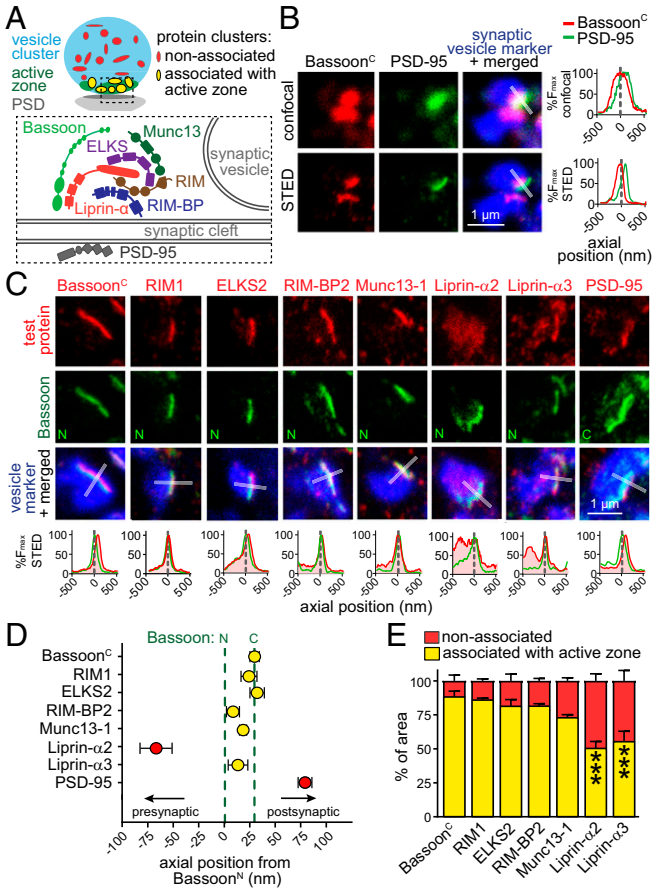

Fig. 1. STED microscopy establishes active-zone localization of Liprin-α3 at excitatory hippocampal synapses. (*A*) Schematic illustration of a synapse. (*B*) Example images of hippocampal excitatory synapses in side view in confocal and STED microscopy stained for Bassoon^{C} and PSD-95. The synaptic vesicle cluster (labeled for synapsin) was imaged by confocal microscopy in all experiments. The intensity profile normalized to peak fluorescence is shown for the profile scan (transparent white rectangle) perpendicular through the center of Bassoon. (*C*) Representative STED images of individual excitatory synapses in side view stained for test proteins, Bassoon, and the vesicle marker vGlut1 (for PSD-95, synapsin antibodies were used due to limitations in antibody compatibility). Fluorescence intensity profiles are shown below. Dashed line at zero indicates the peak localization of Bassoon^{N}. Overview images and confocal scans are provided in Fig. S1. (*D*) Axial positions of test proteins relative to Bassoon^{N}. Bassoon^{N}, n = 920 synapses/8 independent cultures; Bassoon^{C}, n = 231/3; RIM1, n = 130/3; ELKS2, n = 141/3; RIM-BP2, n = 84/3; Munc13-1, n = 92/3; Liprin-α2, n = 105/3; Liprin-α3, n = 234/3; PSD-95, n = 79/3. (*E*) Percentage of test protein clusters associated (yellow) or not associated (red) with the active zone. Bassoon^{C}, n = 985 synapses/5 images/3 independent cultures; RIM1, n = 795/5/3; ELKS2, n = 845/6/3; RIM-BP2, n = 1,298/6/3; Munc13-1, n = 1,935/6/3; Liprin-α2, n = 1,296/6/3; Liprin-α3, n = 1,425/6/3. Statistical significance determined by two-way ANOVA (localization significant at $P \leq 0.001$; test protein not significant, interaction significant at $P \leq 0.001$) followed by Holm–Šídák posttests (reported in figure) comparing each distribution vs. that of Bassoon^{C}. All data are means ± SEM (***$P \leq 0.001$).

density (PSD). We first imaged cultured hippocampal neurons stained with antibodies against the Bassoon N terminus (Bassoon^{N}) or C terminus (Bassoon^{C}), the excitatory PSD marker PSD-95, and a synaptic vesicle protein to identify synapses. We identified synapses in side view (Fig. 1*B* and Fig. S1*A*) by identifying a cluster of synaptic vesicles with an active zone marked by Bassoon appearing as a narrow band (531 ± 25 nm long; n = 45 synapses) at one edge of the vesicle cloud. At these synapses, PSD-95 was opposed to Bassoon and could be reliably separated from Bassoon in STED but not confocal microscopy.

We next analyzed pairwise stainings of synapses in side view for all known active-zone proteins, including Liprin-α2 and Liprin-α3, with Bassoon (Fig. 1 *C* and *D* and Fig. S1). We expressed test protein localization relative to Bassoon^{N} by identifying the peak intensity in line profiles (1 μm long and 250 nm wide) perpendicular through the center of the active zone, and calculated the average peak position from the individual peaks. In this analysis, negative values are proximal to Bassoon^{N} inside the nerve terminal, whereas positive values are distal toward the presynaptic plasma membrane, the synaptic cleft, and the postsynaptic compartment. As observed before with stochastic optical resolution microscopy (STORM) (19), the ∼450-kDa protein Bassoon had an orientation at the active zone with Bassoon^{C} being closer to the plasma membrane than Bassoon^{N} (Fig. 1 *C* and *D*), and the peaks were separated by +30 ± 4 nm. The peak signal of PSD-95, indicating the position of the PSD, was +80 ± 7 nm distal from Bassoon^{N}. The peak fluorescent signals of Liprin-α3, RIM1, Munc13-1, ELKS2, and RIM-BP2, but not of Liprin-α2, were between the peaks of Bassoon^{N} and Bassoon^{C}. These data establish close colocalization of these proteins at the active zone, with the exception of Liprin-α2.

Bassoon, RIM-BP2, RIM1, ELKS2, and Munc13-1 all showed relatively sharp peaks at the active zone. Interestingly, Liprin-α3 had an additional widespread component (Fig. 1*C*) that was localized inside the nerve terminal. This component was pronounced for Liprin-α2 (Fig. 1*C*) with no sharp peak at the active zone, which led to a shift of the average Liprin-α2 peak position toward the inside of the nerve terminal at −67 ± 15 nm relative to Bassoon^{N} (Fig. 1*D*).

To assess the localization of each protein within and outside the active zone, we generated two masks (Fig. 1*A*): one that outlined the nerve terminal (vGlut1 or Synapsin; Fig. 1*A*, blue), and one that defined the active zone (Bassoon^{N}; Fig. 1*A*, green). We then quantified the area associated with the active zone for each protein (Fig. 1*A*, yellow) and compared it vs. the area of the same protein outside the active zone (Fig. 1*A*, red), normalized to the sum of the area of active zone and nonactive zone components (Fig. 1*E*). This provides a measure of signal distribution within a nerve terminal without accounting for the signal intensity within the area. The majority of the area stained for Bassoon^{C}, RIM1, ELKS2, RIM-BP2, and Munc13-1 was at the active zone (73–90%; Fig. 1*E*). Liprin-α2 and Liprin-α3 had ∼50% of positively stained area outside the active zone. Thus, both proteins are widespread in a presynaptic nerve terminal. The key difference between Liprin-α2 and -α3 is that the peak intensity for Liprin-α3 is within the active zone (Fig. 1*D*), whereas the peak of Liprin-α2 is away from other active-zone proteins shifted toward the synaptic vesicle cloud, which arises as an average from its widespread distribution throughout the nerve terminal.

Finally, we tested whether localization of Liprin-α3 depends on other active-zone proteins (Fig. S2). We generated KO neurons for RIM1, RIM2, ELKS1, and ELKS2, which leads to strong disruption of the active zone (20). In this mutant, however, Liprin-α3 synaptic fluorescence and peak localization were not affected, and the line profile peak intensity was only mildly impaired, indicating that active-zone localization of Liprin-α3 is largely independent of RIM and ELKS.

Generation of Liprin-α3–KO Mice. The localization of Liprin-α3 at the active zone suggests that Liprin-α3 may play a role in active-zone function. To test this hypothesis, we generated Liprin-α3–KO mice by using CRISPR/Cas9 gene editing in single-cell zygotes. We selected an allele that had an 8-bp deletion (Fig. 2*A*), inducing a frame-shift mutation leading to nonsense-mediated decay. Heterozygote matings produced offsprings with a Mendelian distribution of homozygote KO (Liprin-α3$^{-/-}$), heterozygote (Liprin-α3$^{+/-}$), and WT (Liprin-α3$^{+/+}$) sibling mice

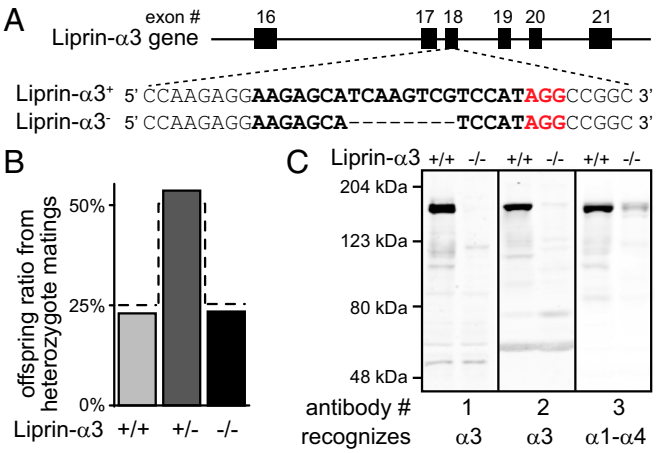

Fig. 2. Generation of Liprin-α3–KO mice. (*A*) CRISPR/Cas9-mediated genome editing in single-cell zygotes. The sgRNA-targeting sequence is shown in bold, the protospacer-adjacent motif (PAM) is red, and the dashed line indicates the deletion. (*B*) Survival analysis of offspring of heterozygous matings. The dashed line represents a Mendelian distribution (n = 418 animals/54 litters). (*C*) Liprin-α3 expression in hippocampi analyzed by fluorescent Western blotting (quantification shown in Fig. S3 *G* and *H*). The Liprin-α3 antibody 3 cross-reacts with Liprin-α1–α4.

(Fig. 2*B*). Western blotting of brain homogenates revealed that Liprin-α3 was removed, and we did not detect bands that would establish the presence of protein fragments (Fig. 2*C*). Liprin-α3$^{-/-}$ mice were viable and fertile, but had a significantly increased distance traveled and were less spatially confined in an open-field assessment of locomotion (Fig. S3 *A–D*), suggesting alterations in brain function. No changes beyond removal of Liprin-α3 were detected when we assessed morphology and protein composition in hippocampi of Liprin-α3$^{-/-}$ mice (Fig. S3 *E–H*).

Impaired Synaptic Vesicle Exocytosis in Liprin-α3$^{-/-}$ Mice. We assessed synaptic transmission in Liprin-α3$^{-/-}$ and Liprin-α3$^{+/+}$ neurons cultured from hippocampi of littermate newborn mice. We first measured AMPA receptor-mediated miniature excitatory postsynaptic currents (mEPSCs; Fig. 3 *A* and *B*). The mEPSC amplitudes and kinetics were indistinguishable between the two genotypes. There was a ∼20% trend toward a reduction in mEPSC frequency, which was not statistically significant. These results indicate that postsynaptic AMPA receptor numbers are not strongly affected by Liprin-α3 KO. Given that previous studies found developmental and postsynaptic roles for Liprin-α, we decided to measure exocytosis of synaptic vesicles directly. We used imaging of synaptic-vesicle cycling upon lentiviral expression of synaptophysin-pHluorin (sypHy; Fig. 3 *C–J*). We compared exocytosis of synaptic vesicles, as indicated by an increase in pHluorin fluorescence, in Liprin-α3$^{+/+}$ neurons, Liprin-α3$^{-/-}$ neurons, and Liprin-α3$^{-/-}$ neurons transduced with a lentivirus that expressed HA-tagged Liprin-α3 from a neuron-specific human synapsin promoter. In hippocampal neurons, Liprin-α3 is expressed as early as day in vitro (DIV) 1 (Fig. S4*A*). To mimic this early expression, we transduced Liprin-α3$^{-/-}$ neurons for rescue with a Liprin-α3–expressing lentivirus at DIV 1. Rescue Liprin-α3 was localized normally as assessed by STED microscopy (Fig. S4 *B–D*). Neurons were stimulated with 40 or 200 action potentials at 20 Hz, followed by application of NH_4Cl to unquench pHluorin fluorescence. No differences in the number of pHluorin-positive or NH_4Cl-responsive puncta was observed across conditions (Fig. S5), indicating that removing or reexpressing Liprin-α3 did not change synapse numbers.

Removal of Liprin-α3 led to a decrease in the number of synapses responsive to action potentials (Fig. 3 *C* and *D*). At responsive synapses, KO of Liprin-α3 was accompanied by a 38% or 46% decrease in pHluorin fluorescence after stimulation with 40 or 200 action potentials, respectively (Fig. 3 *E–J*). Upon

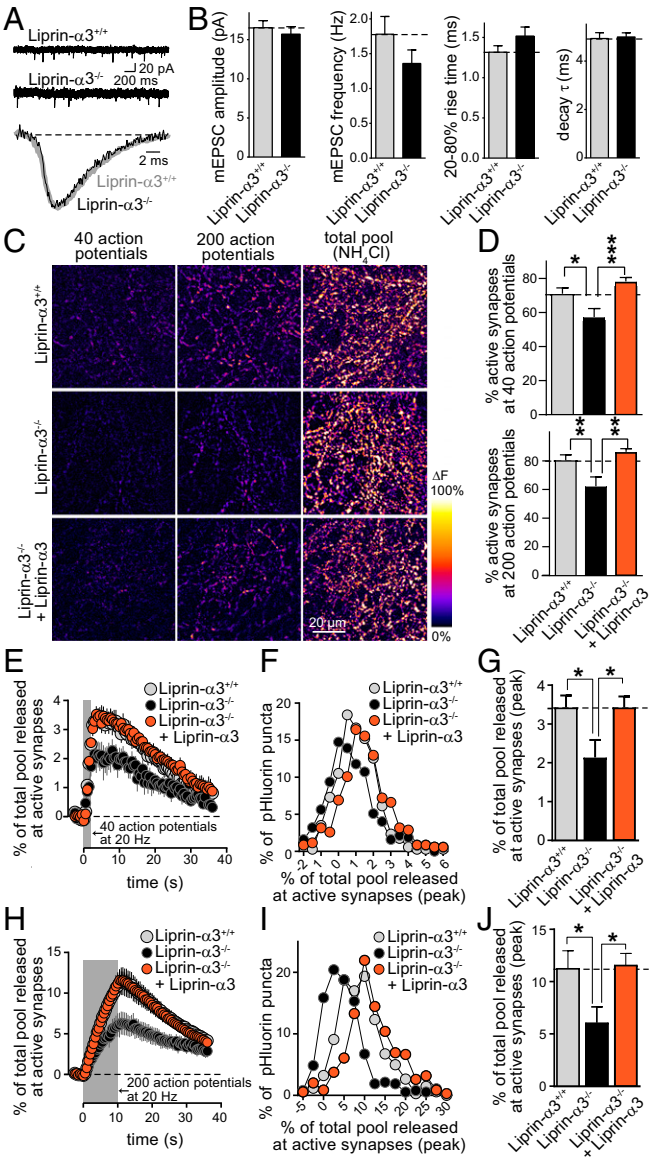

Fig. 3. Synaptic vesicle exocytosis is impaired upon Liprin-α3 KO. (*A* and *B*) Example traces (*A*) and quantification (*B*) of mEPSCs. Liprin-α3$^{+/+}$, n = 47 cells/4 independent cultures; Liprin-α3$^{-/-}$, n = 48/4. (*C*) Pseudocolored images of peak fluorescence change in sypHy-expressing Liprin-α3$^{+/+}$ neurons, Liprin-α3$^{-/-}$ neurons, and Liprin-α3$^{-/-}$ neurons rescued with lentiviral expression of Liprin-α3 transduced at DIV 1. Neurons were stimulated with 40 or 200 action potentials and dequenched with NH_4Cl. (*D*) Quantification of the percentage of sypHy puncta responsive to 40 (*Top*) or 200 (*Bottom*) action potentials. (*E–G*) Quantification of sypHy mean fluorescence changes at active synapses stimulated with 40 action potentials expressed as percentage of the NH_4Cl-responsive vesicle pool (*E*), and the frequency distribution (*F*) and peak response (*G*) of the same data. Liprin-α3$^{+/+}$, n = 2,365 NH_4Cl-responsive synapses/1,338 active synapses/11 coverslips/6 independent cultures; Liprin-α3$^{-/-}$ 2,371/1,093/11/6; Liprin-α3$^{-/-}$ + Liprin-α3, n = 2,438/1,463/11/6. (*H–J*) Quantification as in *E–G* but for neurons stimulated with 200 action potentials. Liprin-α3$^{+/+}$, n = 2,353/1,485/11/6; Liprin-α3$^{-/-}$, n = 2,346/1,164/11/6; Liprin-α3$^{-/-}$ + Liprin-α3, n = 2,427/1,598/11/6. All data are means ± SEM [*$P \leq$ 0.05, **$P \leq$ 0.01, and ***$P \leq$ 0.001, Student's t tests (*B*; all $P > 0.05$) or one-way ANOVA (*D*, *G*, and *J*) followed by Holm–Šídák multiple comparisons test comparing each condition vs. Liprin-α3$^{-/-}$]. The number of coverslips was used as a basis for statistics in sypHy imaging.

reexpression of Liprin-α3, release recovered to levels that were indistinguishable from WT littermate neurons. Efficient Liprin-α3 expression and rescue of its function required viral transduction early after plating (Fig. S6). These experiments establish a defect in synaptic vesicle exocytosis upon loss of Liprin-α3. The full rescue indicates that the impairment in exocytosis is caused by loss of Liprin-α3 in the mutant mice, and the reversibility of the impairment establishes that postnatal, neuronal expression of Liprin-α3 is sufficient to mediate its role in exocytosis. Together with the presynaptic localization observed with STED microscopy, these experiments establish a presynaptic function of Liprin-α3 to enhance synaptic strength. Field recordings in acute brain slices confirmed a defect in synaptic strength in excitatory Schaffer collateral to CA1 synapses of the hippocampus (Fig. S7).

Synaptic Ultrastructure in Liprin-α3–KO Neurons. To determine whether Liprin-α3 has a structural role in vertebrate presynaptic morphogenesis, we pursued EM analysis of synapse structure in cultured hippocampal neurons after chemical fixation (Fig. 4 *A*–*G*). We observed a 23% loss of vesicles docked to the presynaptic plasma membrane upon KO of Liprin-α3, accompanied by a 25% loss of vesicles within 100 nm of the target membrane, referred to as tethered vesicles (Fig. 4 *E* and *F*). Bouton size, PSD length, and the number of vesicles per bouton were not changed.

Chemical fixation leads to collapse of intra- and extracellular space, potentially confounding the analysis of synaptic ultrastructure. We therefore repeated this experiment with the use of high-pressure freezing followed by freeze substitution, directly comparing the two methods and the Liprin-α3–KO phenotypes (Fig. 4 *H*–*M*). Liprin-α3–KO phenotypes were essentially the same, with a 30% and 24% loss of docked and tethered vesicles, respectively. In addition, we observed a small decrease in bouton size and PSD length upon Liprin-α3 KO, perhaps suggesting mild structural roles for Liprin-α3 in bouton formation.

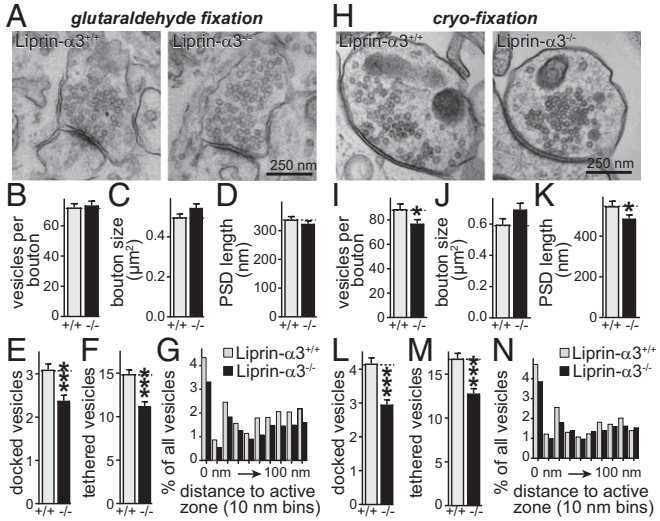

Fig. 4. Impaired synaptic vesicle docking and tethering after Liprin-α3 KO. (*A*) Representative EM images of synapses of cultured hippocampal neurons fixed with glutaraldehyde. (*B*–*F*) Quantification of vesicles per bouton (*B*), bouton size (*C*), PSD length (*D*), docked vesicles (*E*), and vesicles tethered within 100 nm (*F*). Liprin-α3$^{+/+}$, n = 150 synapses/3 independent cultures; Liprin-α3$^{-/-}$, n = 147/3. (*G*) Histogram of the vesicle distribution in the first 100 nm of the active zone in 10-nm bins expressed as a percentage of all synaptic vesicles. Numbers of synapses and cultures are as in *B*–*F*. (*H*–*N*) Same as *A*–*G*, but for neurons cryofixed by high-pressure freezing. Liprin-α3$^{+/+}$, n = 104/3; Liprin-α3$^{-/-}$, n = 121/3. Data are means ± SEM unless stated otherwise (*$P \leq 0.05$ and ***$P \leq 0.001$, unpaired Student's t test).

Deficits in vesicle docking are often accompanied by accumulation of nondocked vesicles within 10–20 nm of the presynaptic plasma membrane, for example in Munc13 and SNARE mutants (21). The decrease in the number of tethered vesicles (Fig. 4 *F* and *M*) suggested that this is not the case in Liprin-α3–KO neurons. To better analyze this, we plotted histograms of the distribution of vesicles within 100 nm of the presynaptic membrane in 10-nm bins (Fig. 4 *G* and *N*). We did not observe an accumulation of undocked vesicles near the plasma membrane, but, instead, mild reductions of vesicles were present across the first 100 nm, establishing a synaptic vesicle tethering defect.

Altered Active-Zone Structure upon Deletion of Liprin-α3. To assess whether Liprin-α3 KO induced structural changes in the active zone, we compared Liprin-α3$^{+/+}$ with Liprin-α3$^{-/-}$ synapses by STED microscopy (Fig. 5 and Fig. S8). Compellingly, at Liprin-α3$^{-/-}$ synapses, the peak of Liprin-α2 staining moved to a position between the Bassoon N and C termini, akin to the localization of Liprin-α3 (Fig. 5*B*). Hence, only upon deletion of Liprin-α3, Liprin-α2 is strongly localized to the active zone. Liprin-α2, however, cannot functionally compensate for the loss of Liprin-α3 because vesicle docking, tethering, and release are impaired at Liprin-α3$^{-/-}$ synapses despite translocation of Liprin-α2 to the active zone. Effects on other active-zone proteins were mild. For each active-zone protein, the peak localization was not affected in Liprin-α3–KO mice (Fig. 5*B*). Nevertheless, we observed modest changes in Bassoon and Munc13-1 labeling (Fig. 5*C* and Figs. S8 and S9). These changes likely reflect rearrangements of the release-site structure that contribute to the impairment in synaptic vesicle tethering, docking, and exocytosis.

Discussion

The localization and function of vertebrate Liprin-α has been uncertain, and pre-, post-, and extrasynaptic functions have been proposed. We establish here that localization of Liprin-α3, but not Liprin-α2, peaks at the active zone (Fig. 1). We find that Liprin-α3 is important for synaptic vesicle docking and release (Figs. 2–4), functions that are likely mediated by a role for Liprin-α3 in determining active-zone composition (Fig. 5). Hence, Liprin-α3 functions at the presynaptic active zone to enhance synaptic strength.

Analysis of Active-Zone Protein Localization at Vertebrate Synapses Using STED Microscopy. A large body of literature suggests that Piccolo/Bassoon, RIM, Munc13, ELKS, RIM-BP, and Liprin-α define the active zone at vertebrate synapses, with biochemical and morphological evidence in support of active-zone association. Although localization was typically established by qualitative immuno-EM, colocalization with other active-zone proteins at a nanoscale has not been systematically studied. Recent advances in superresolution microscopy provide new tools to tackle this limitation. A first study employed STORM microscopy and found colocalization of Bassoon/Piccolo and RIM (19). Two recent papers provided additional evidence for active-zone localization of RIM-BP, Bassoon, and Munc13 by using STED or STORM microscopy (22, 23). Here we extend these studies by systematic mapping of active-zone protein localization, including vertebrate ELKS and Liprin-α, proteins that have not been studied by using superresolution microscopy to our knowledge. We find that members of each protein family localize to the active zone and are opposed to the PSD at excitatory hippocampal synapses. Notably, the peaks of RIM-BP2, Liprin-α3, Munc13-1, RIM1, and ELKS2 all fall within the 25 nm between the Bassoon N and C termini, strongly supporting that these proteins are associated with one another at active zones.

Our work relates to comprehensive studies at the fly neuromuscular junction, where STED microscopy has revealed that Brp, a partial homolog of ELKS, forms prominent umbrella-shaped

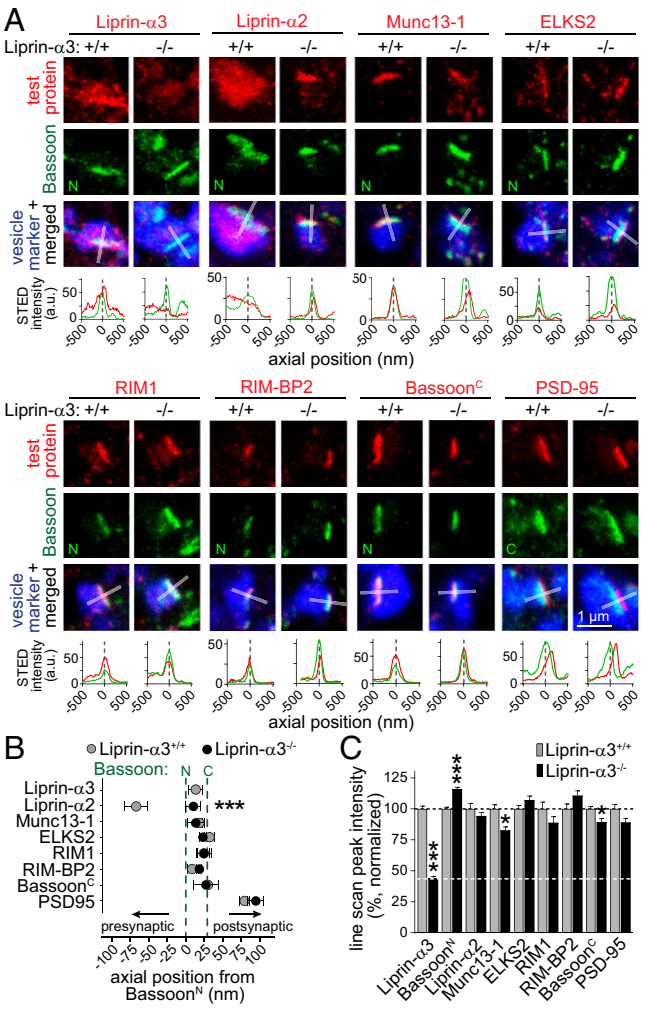

Fig. 5. STED analysis of Liprin-α3–KO synapses. (*A*) Representative STED images of side-view synapses and line profiles [as in Fig. 1 but showing arbitrary units (a.u.)]. (*B*) Axial positions of the test proteins relative to Bassoon: Bassoon^{N} ($^{+/+}$, $n = 841/8$; $^{-/-}$, $n = 817/8$); Liprin-α3 ($^{+/+}$, $n = 234/3$); Liprin-α2 ($^{+/+}$, $n = 105/3$; $^{-/-}$, $n = 120/3$); Bassoon^{C} ($^{+/+}$, $n = 55/3$; $^{-/-}$, $n = 28/3$); Munc13-1 ($^{+/+}$, $n = 92/3$; $^{-/-}$, $n = 77/3$); ELKS2 ($^{+/+}$, $n = 141/3$; $^{-/-}$, $n = 196/3$); RIM1 ($^{+/+}$, $n = 130/3$; $^{-/-}$, $n = 114/3$); RIM-BP2 ($^{+/+}$, $n = 84/3$; $^{-/-}$, $n = 107/3$); and PSD-95 ($^{+/+}$, $n = 79/3$; $^{-/-}$, $n = 116/3$). Statistical significance determined by two-way ANOVA (genotype significant at $P \leq 0.05$; test protein significant at $P \leq 0.001$; interaction significant at $P \leq 0.001$) followed by Holm–Šídák multiple-comparisons posttests (reported in figure). (*C*) Peak intensity of line profiles normalized to the average of Liprin-α3$^{+/+}$ synapses: Liprin-α3 ($^{+/+}$, $n = 234/3$; $^{-/-}$, $n = 175/3$); Bassoon^{N} ($^{+/+}$, $n = 772/8$; $^{-/-}$, $n = 805/8$); Liprin-α2 ($^{+/+}$, $n = 105/3$; $^{-/-}$, $n = 120/3$); Bassoon^{C} ($^{+/+}$, $n = 231/3$; $^{-/-}$, $n = 169/3$); Munc13-1 ($^{+/+}$, $n = 92/3$; $^{-/-}$, $n = 77/3$); ELKS2 ($^{+/+}$, $n = 141/3$; $^{-/-}$, $n = 175/3$); RIM1 ($^{+/+}$, $n = 130/3$; $^{-/-}$, $n = 114/3$); RIM-BP2 ($^{+/+}$, $n = 84/3$; $^{-/-}$, $n = 107/3$); and PSD-95 ($^{+/+}$, $n = 116/3$; $^{-/-}$, $n = 158/3$). Statistical significance determined by two-way ANOVA (genotype not significant; test protein significant at $P \leq 0.001$; interaction significant at $P \leq 0.001$) followed by Holm–Šídák multiple-comparisons posttests (reported in figure). All data are means ± SEM (*$P \leq 0.05$ and ***$P \leq 0.001$). The data were acquired simultaneously with identical settings in a blind experiment in Liprin-α3$^{+/+}$ control and Liprin-α3$^{-/-}$ neurons, and the Liprin-α3$^{+/+}$ data are the same data that are shown in Fig. 1. A second, independent assessment of active-zone protein localization is shown in Fig. S2. Overview images and additional analyses are in Figs. S8 and S9.

T-bars that reach 200–300 nm into the nerve terminal. The fly homologs of RIM-BP, Liprin-α, and Munc13 each form small, distinct clusters surrounding the base of these T-bars (1, 18, 24). Our data at hippocampal synapses suggest finer subclustering of active-zone proteins, resulting in relatively homogenous appearance of the active zone in STED microscopy. A contributing factor could be that hippocampal synapses are more diverse and likely less stereotyped than the fly neuromuscular junction.

Liprin-α3 as an Active-Zone Scaffold. Our data firmly establish presynaptic localization and function of Liprin-α3. However, several observations set Liprin-α3 apart from other active-zone proteins. First, Liprin-α3 has a broader distribution than other active-zone proteins, with antibody staining spread throughout the nerve terminal (Fig. 1). Second, at synapses that lack RIM and ELKS, Liprin-α3 localization is more mildly affected than that of other active-zone proteins (20) (Fig. S2). The most parsimonious model is that interactions with LAR-PTPs and Liprin-α self-association play roles in Liprin-α targeting and presynaptic assembly (2, 11). Studies of active-zone assembly in *C. elegans* suggested that Liprin-α may act early in active-zone assembly (6, 7, 25), and fit with our finding that Liprin-α3 is recruited to the presynaptic plasma membrane independent of RIM and ELKS. In invertebrates, syd-1 is required upstream of Liprin-α/syd-2, and overexpression of Liprin-α/syd-2 bypasses the need for syd-1 (26, 27). This suggested that syd-1 may recruit Liprin-α/syd-2 to synapses. Vertebrates express only distal orthologs of syd-1, called SYD1A/syde1 and SYD1B/syde2, with a Rho-GAP activity that is not present in invertebrate syd-1 but essential for cytoskeletal remodeling in vertebrates (28, 29), and localization of the vertebrate orthologs is not known. Future studies are necessary to address potential roles of LAR-RPTPs and SYD1A/B for targeting Liprin-α3 to vertebrate active zones.

Our functional and morphological data support a scaffolding role for Liprin-α3. We observe a loss of tethered and docked synaptic vesicles that is well matched with a reduction in exocytosis. Although recent studies at the fly neuromuscular junction support roles for Liprin-α in targeting of a specific Munc13 isoform (24), there is currently no support for a direct interaction between Liprin-α3 and Munc13. Because the reduction of Munc13 levels at Liprin-α3$^{-/-}$ synapses is mild, and because Liprin-α3$^{-/-}$ synapses have a loss in docked and tethered vesicles [tethered vesicles are increased in Munc13-KO synapses (21)], it is unlikely that the secretory deficit in Liprin-α3$^{-/-}$ synapses is the result of an isolated loss of Munc13. Instead, the exocytotic defect is probably a result of a combination of active-zone defects caused by a loss of scaffolding by Liprin-α3.

Redundant and Diverse Roles for Vertebrate Liprin-α in Brain Development and Function. Although our studies establish localization and function of Liprin-α3 at the presynaptic active zone, they do not exclude other roles for Liprin-α3, for example, in cellular transport or morphogenesis, as generally suggested for Liprin-αs from biochemical studies and invertebrate genetics (1, 9, 10). Our data, however, suggest that these roles are not essential or are compensated for by other Liprin-αs, because Liprin-α3–KO mice survive and develop mostly normally (Fig. 2 and Fig. S3).

Diverse roles for Liprin-α are also strongly supported by the variable localization of the various Liprin-α proteins within neurons and by studies in nonneuronal cells. Within neurons, Liprin-α1 is mostly localized dendritically, and knockdown and overexpression experiments support roles in dendrite morphogenesis (14, 15, 30). These functions are consistent with studies in nonneuronal cells, where Liprin-α1 controls edge dynamics in motile cancer cells through focal adhesion (31). Liprin-α2 localization appears more restricted to synapses, but, so far, it was unclear whether it is pre- or postsynaptically localized (14–16). A functional study using knockdown of Liprin-α2 suggested a presynaptic function in regulating the localization and turnover of other presynaptic proteins to control release (17). Together with the widespread presynaptic localization established here, these data suggest that one function of Liprin-α2 may be the trafficking

and/or capture of presynaptic components, consistent with roles of Dliprin-α in flies (9).

Our data reveal insight into the interplay between Liprin-α2 and Liprin-α3. Compellingly, when Liprin-α3 was removed, Liprin-α2 translocated to the active zone, mimicking the localization of Liprin-α3. There are several potential alternative explanations. First, it is possible that a limited number of Liprin-α binding sites at the active zone accounts for this interplay, and Liprin-α3 outcompetes Liprin-α2 for localization because it is expressed higher or has a higher affinity for key interacting partners. Similar mechanisms were observed for presynaptic Ca^{2+} channels, which compete for a limited number of slots (32). Alternatively, Liprin-α3 could have an active role in suppressing active-zone localization of Liprin-α2, for example, by recruiting proteins that inhibit Liprin-α2 active-zone localization. Finally, Liprin-α3 expression may suppress Liprin-α2 expression and therefore its active-zone levels. This is unlikely because there is no strong increase in Liprin-α2 expression in Liprin-α3–KO animals. Regardless of the mechanism, our data indicate that the functions of Liprin-α3 are not identical to those of Liprin-α2 because Liprin-α3$^{-/-}$ neurons have a secretory impairment that is not compensated for by Liprin-α2. A previous study complements this point: Liprin-α3 cannot fully compensate for knockdown of Liprin-α2 (17). Future studies are needed to generate KO mice for Liprin-α2 and other Liprin-αs and to systematically compare single- and double-KO phenotypes. Together, this and previous studies support diverse roles for Liprin-α in morphogenesis, cellular trafficking, and synaptic transmission. These roles are shared by a single gene in invertebrates, they have likely diverged across several Liprin-α genes in vertebrates.

Methods

Mice. The constitutive Liprin-α3–KO mice were generated by CRISPR/Cas9 gene editing in one-cell zygotes. All animal experiments were performed according to institutional regulations at Harvard University.

Neuronal Cultures. Primary mouse hippocampal cultures were generated from newborns as previously described (20), and all analyses were performed at DIV 14–17.

Morphology. Confocal and STED experiments were performed with a Leica SP8 Confocal/STED 3× microscope, and detailed information is outlined in *SI Methods*. For transmission EM, neuronal cultures were fixed with glutaraldehyde or frozen with a Leica EM ICE high-pressure freezer. Tissue processing, imaging, and data analyses were performed as described previously (20). All experiments were done by an experimenter blind to the genotype.

Electrophysiology and Imaging. mEPSC recordings and sypHy imaging experiments were performed in cultured neurons at DIV 14–17. SypHy was delivered by lentiviral infection. All experiments were done by an experimenter blind to the genotype.

ACKNOWLEDGMENTS. We thank L. Bickford, J. Wang, E. Atwater, and M. Sanghvi for technical assistance; Dr. A. deJong, Dr. W. Regehr, and R. Held for comments; Drs. T. Südhof and S. Schoch for antibodies; and Drs. M. Verhage and J. Broeke for a MATLAB program to analyze EM images. This work was supported by National Institutes of Health (NIH) Grants R01NS083898 and R01MH113349 (to P.S.K.); the Brain Research Foundation (P.S.K.); the Harvard Brain Initiative (P.S.K.); the Armenise Harvard Foundation (P.S.K.); fellowships from the Croucher Foundation (to M.Y.W.) and the Lefler Foundation (to M.Y.W.); the Brooks, Fix and Gordon Fellowship Funds (to C.L.); and National Science Foundation graduate research fellowship DGE1144152 (to S.S.H.W.). The following Harvard Medical School core facilities supported this project: Neurobiology Imaging (supported by NIH Grant P30NS072030), Conventional Electron Microscopy, the Neurodiscovery Center, and the Transgenic Cores at Brigham Women's and Boston Children's Hospital (Intellectual and Developmental Disabilities Research Center, supported by NIH Grant P30HD18655).

1. Südhof TC (2012) The presynaptic active zone. *Neuron* 75:11–25.
2. Serra-Pagès C, Medley QG, Tang M, Hart A, Streuli M (1998) Liprins, a family of LAR transmembrane protein-tyrosine phosphatase-interacting proteins. *J Biol Chem* 273:15611–15620.
3. Schoch S, et al. (2002) RIM1alpha forms a protein scaffold for regulating neurotransmitter release at the active zone. *Nature* 415:321–326.
4. Ko J, Na M, Kim S, Lee JR, Kim E (2003) Interaction of the ERC family of RIM-binding proteins with the Liprin-alpha family of multidomain proteins. *J Biol Chem* 278:42377–42385.
5. Zhen M, Jin Y (1999) The Liprin protein SYD-2 regulates the differentiation of presynaptic termini in C. elegans. *Nature* 401:371–375.
6. Dai Y, et al. (2006) SYD-2 Liprin-alpha organizes presynaptic active zone formation through ELKS. *Nat Neurosci* 9:1479–1487.
7. Chia PH, Patel MR, Wagner OI, Klopfenstein DR, Shen K (2013) Intramolecular regulation of presynaptic scaffold protein SYD-2/Liprin-α. *Mol Cell Neurosci* 56:76–84.
8. Astigarraga S, Hofmeyer K, Farajian R, Treisman JE (2010) Three Drosophila Liprins interact to control synapse formation. *J Neurosci* 30:15358–15368.
9. Miller KE, et al. (2005) Direct observation demonstrates that Liprin-alpha is required for trafficking of synaptic vesicles. *Curr Biol* 15:684–689.
10. Choe K-M, Prakash S, Bright A, Clandinin TR (2006) Liprin-alpha is required for photoreceptor target selection in Drosophila. *Proc Natl Acad Sci USA* 103:11601–11606.
11. Taru H, Jin Y (2011) The Liprin homology domain is essential for the homomeric interaction of SYD-2/Liprin-α protein in presynaptic assembly. *J Neurosci* 31:16261–16268.
12. Patel MR, Shen K (2009) RSY-1 is a local inhibitor of presynaptic assembly in C. elegans. *Science* 323:1500–1503.
13. Zürner M, Schoch S (2009) The mouse and human Liprin-alpha family of scaffolding proteins: Genomic organization, expression profiling and regulation by alternative splicing. *Genomics* 93:243–253.
14. Zürner M, Mittelstaedt T, tom Dieck S, Becker A, Schoch S (2011) Analyses of the spatiotemporal expression and subcellular localization of Liprin-α proteins. *J Comp Neurol* 519:3019–3039.
15. Spangler SA, et al. (2011) Differential expression of Liprin-α family proteins in the brain suggests functional diversification. *J Comp Neurol* 519:3040–3060.
16. Wyszynski M, et al. (2002) Interaction between GRIP and Liprin-alpha/SYD2 is required for AMPA receptor targeting. *Neuron* 34:39–52.
17. Spangler SA, et al. (2013) Liprin-α2 promotes the presynaptic recruitment and turnover of RIM1/CASK to facilitate synaptic transmission. *J Cell Biol* 201:915–928.
18. Fouquet W, et al. (2009) Maturation of active zone assembly by Drosophila Bruchpilot. *J Cell Biol* 186:129–145.
19. Dani A, Huang B, Bergan J, Dulac C, Zhuang X (2010) Superresolution imaging of chemical synapses in the brain. *Neuron* 68:843–856.
20. Wang SSH, et al. (2016) Fusion competent synaptic vesicles persist upon active zone disruption and loss of vesicle docking. *Neuron* 91:777–791.
21. Imig C, et al. (2014) The morphological and molecular nature of synaptic vesicle priming at presynaptic active zones. *Neuron* 84:416–431.
22. Tang A-H, et al. (2016) A trans-synaptic nanocolumn aligns neurotransmitter release to receptors. *Nature* 536:210–214.
23. Grauel MK, et al. (2016) RIM-binding protein 2 regulates release probability by fine-tuning calcium channel localization at murine hippocampal synapses. *Proc Natl Acad Sci USA* 113:11615–11620.
24. Böhme MA, et al. (2016) Active zone scaffolds differentially accumulate Unc13 isoforms to tune Ca(2+) channel-vesicle coupling. *Nat Neurosci* 19:1311–1320.
25. Ackley BD, et al. (2005) The two isoforms of the Caenorhabditis elegans leukocyte-common antigen related receptor tyrosine phosphatase PTP-3 function independently in axon guidance and synapse formation. *J Neurosci* 25:7517–7528.
26. Owald D, et al. (2010) A Syd-1 homologue regulates pre- and postsynaptic maturation in Drosophila. *J Cell Biol* 188:565–579.
27. Patel MR, et al. (2006) Hierarchical assembly of presynaptic components in defined C. elegans synapses. *Nat Neurosci* 9:1488–1498.
28. Wentzel C, et al. (2013) mSYD1A, a mammalian synapse-defective-1 protein, regulates synaptogenic signaling and vesicle docking. *Neuron* 78:1012–1023.
29. Lo HF, et al. (2017) Association of dysfunctional synapse defective 1 (SYDE1) with restricted fetal growth - SYDE1 regulates placental cell migration and invasion. *J Pathol* 241:324–336.
30. Hoogenraad CC, et al. (2007) Liprinalpha1 degradation by calcium/calmodulin-dependent protein kinase II regulates LAR receptor tyrosine phosphatase distribution and dendrite development. *Dev Cell* 12:587–602.
31. Astro V, et al. (2016) Liprin-α1 and ERC1 control cell edge dynamics by promoting focal adhesion turnover. *Sci Rep* 6:33653.
32. Cao YQ, et al. (2004) Presynaptic Ca2+ channels compete for channel type-preferring slots in altered neurotransmission arising from Ca2+ channelopathy. *Neuron* 43:387–400.

Supporting Information

Wong et al. 10.1073/pnas.1719012115

SI Methods

Mouse Lines. The conditional RIM1/2 × ELKS1/2 quadruple homozygous KO mice were previously characterized (1) and were generated by crossing conditional RIM1 (2) (RRID:IMSR_JAX:015832), RIM2 (3) (RRID:IMSR_JAX:015833), ELKS1 (4) (RRID:IMSR_JAX:015830), and ELKS2 (5) (RRID:IMSR_JAX:015831)-KO mice. The constitutive Liprin-α3–KO mice were generated as described here later. All animal experiments were performed according to institutional regulations at Harvard University.

Generation of Liprin-α3–KO Mice. Liprin-α3–KO mice were generated for this study by CRISPR/Cas9 gene editing in one-cell zygotes (6). We first identified several 20-bp-long potential targeting sequences followed by PAM sequences in multiple exons of the *Ppfia3* gene, which encodes Liprin-α3, and tested their efficiency in mouse 3T3 cells by using transfection followed by surveyor assays. We selected a targeting sequence in exon 18 based on its efficiency in disrupting the Liprin-α3 gene in cultured cells. Cas9 mRNA, single guide RNA (sgRNA), and donor oligos were then prepared for zygote injections. The bicistronic expression vector expressing Cas9 and an sgRNA (pX330-U6-Chimeric_BB-CBh-hSpCas9) was obtained from Addgene (plasmid no. 42230). Targeting oligos for exon 18 of the mouse *Ppfia3* gene encoding Liprin-α3 (5′-CACCGAAGAGCATCAAGTCGTCCAT-3′and 5′- AAACATGGACGACTTGATGCTCTTC-3′) were annealed, phosphorylated, and ligated into the linearized pX330 vector. PCR amplification was performed to add a T7 promoter to the Cas9 coding region with primers 5′-TAATACGACTCACTATAGGGagaATGTACCCATACGATGTTCC-3′ and 5′-GCGAGCTCTAGGAATTCTTAC-3′. The T7 promoter was added to the sgRNA by using PCR with primers 5′TAATACGACTCACTATAGGAAGAGCATCAAGTCGTCCAT-3′ and 5′-AAAAGCACCGACTCGGTGCC-3′. T7-Cas9 and T7-sgRNA PCR products were gel-purified and used as the template for in vitro transcription by using the mMESSAGE mMACHINE T7 ULTRA kit (Life Technologies) and the MEGAshortscript T7 kit (Life Technologies), respectively. Cas9 mRNA and sgRNAs were purified by using the MEGAclear kit (Life Technologies), eluted with nuclease-free water, and size-validated by denaturing agarose gel and urea Tris-boric acid-EDTA polyacrylamide gel electrophoresis, respectively. Cas9 mRNAs (5 ng/μL) and sgRNA (2.5 ng/μL) and a donor oligo (10 ng/μL) were freshly mixed in nuclease-free water and injected directly into the pronucleus of one-cell zygotes of FVB/NCrl mice. Injections were carried out in the Brigham & Women's Hospital Transgenic Mouse Core Facility at Harvard Medical School. The zygotes were immediately transplanted into foster mothers. The offspring of the zygote injections were genotyped by a PCR-based Surveyor assay (Transgenomic) with primers 5′- TGCCCGTCTTGAGAGGATGG-3′ and 5′- AAAGAGAATCCTGGGACAGC-3′ to screen for founder lines that carry insertions or deletions (indels) at the targeting locus. We identified three founders in 142 offspring by PCR and Surveyor assay. Exon 18 of indel-carrying founders was amplified by PCR, subcloned, and sequenced to identify specific mutations. In each founder, we cloned PCR fragments of the targeted gene locus and sequenced them. We detected as many as three different alleles in each founder, suggesting that gene editing continued to occur beyond the single-cell stage. A frame-shift mutation deleting 8 bp was selected, removal of Liprin-α3 was confirmed by Western blot, and the allele was then outbred to 129S2/SvPasCrl mice for five generations and maintained as heterozygous line. The mice were genotyped by using oligos 5′-GATCTTCAAGCCAGTTCTGC-3′ and 5′-AGAGCCGGCCTATGGACGAC-3′ for the WT allele (resulting in a 365-bp band) and oligos 5′-GATCTTCAAGCCAGTTCTGC-3′ and 5′-GAGCCGGCCTATGGATGCTC-3′ for the mutant allele (resulting in a 356-bp band). All experiments were performed on littermate pairs of WT Liprin-α3$^{+/+}$ and Liprin-α3$^{-/-}$ mice.

Cell Cultures and Lentiviral Infection. Primary mouse hippocampal cultures were generated from newborns within 48 h after birth as previously described (1, 4). Unless otherwise stated, neurons were plated on 0.15-mm-thick chemically stripped glass coverslips. Neurons from conditional RIM1/2 × ELKS1/2 quadruple homozygous floxed mice were infected at 5 DIV with viruses expressing a cre recombinase (to generate cKO^{R+E} neurons) or an inactive cre truncation mutant (to generate control^{R+E} neurons) under the human synapsin promoter (1). Lentiviruses were generated in HEK293T cells by Ca^{2+} phosphate transfection. HEK cell supernatants containing cre-expressing and control viruses were collected 2 d after transfection and applied to cultures at 5 DIV. Liprin-α3$^{-/-}$ and Liprin-α3$^{+/+}$ cultures were generated from littermates of heterozygote breeding pairs that were genotyped before culturing. For sypHy imaging, a sypHyA4-expressing lentivirus (1, 7) and an SV2-tdTomato–expressing lentivirus were applied to cultures at DIV 3. Lentiviruses expressing a synapsin promoter-driven, N-terminally HA-tagged rat Liprin-α3 were applied to cultures at DIV 1 (Fig. 3 and Figs. S4 and S5) or at DIV 5 (Fig. S6) for rescue experiments.

Western Blotting. Fluorescent Western blotting was used for quantitative protein-expression analyses in hippocampal lysates. Hippocampi were collected from 3–4-wk-old littermate Liprin-α3$^{+/+}$ and Liprin-α3$^{-/-}$ mice, flash-frozen, and homogenized by using a motorized glass–Teflon homogenizer in a buffer containing 150 mM NaCl, 25 mM Hepes, pH 7.5, 4 mM EDTA, 1 mM DTT, 1 mM PMSF, 1 μg/mL Leupeptin, Pepstatin, 2 μg/mL Aprotinin, and 1× PhosStop (Roche), and extracted in 1% Triton for 1 h at 4 °C. Protein concentration was measured by a bicinchoninic acid assay. Protein (20 μg per sample) was run on SDS/PAGE gels and transferred onto nitrocellulose membranes. Blots were washed with Tris-buffered saline (TBS) solution, blocked in TBS solution containing 5% milk, 5% goat serum, and then incubated with primary antibodies overnight at 4 °C in TBS solution containing 5% BSA and 0.1% Tween-20. Fluorescent secondary antibody incubation was done for 1 h at room temperature. Membranes were washed in TBS solution and air-dried before imaging. Membranes were scanned by using a LI-COR Odyssey Fluorescent Scanner, and quantification was done by using ImageJ on the original 16-bit images. The fluorescent signal of the test protein band was normalized to a β-actin loading control that was run in the same lane, and protein levels were expressed normalized to the average of the three WT control samples. For display of fluorescent Western blots, the 16-bit images were converted to 8-bit images, which resulted in limited loss of background information in image areas with very low background, but reflects the overall relationship between background and signal well. All analyses were done in at least three independent littermate pairs.

For nonquantitative assessment of rescue construct expression in cultured hippocampal neurons, chemiluminescent Western blotting was used to detect Liprin-α3. Cultured neurons from one coverslip were harvested in 25 μL 1× SDS sample buffer and run on 7.5% SDS gels followed by transfer to nitrocellulose membranes. Membranes were blocked in TBS solution containing 10% nonfat milk with 5% goat serum and 0.1% Tween-20 for 1 h at room temperature.

Membranes were incubated overnight at 4 °C in primary antibodies in TBS solution with 5% nonfat milk, 2.5% goat serum, and 0.1% Tween-20. Membranes were incubated with HRP-conjugated secondary antibodies (1:10,000) at room temperature for 2 h. Membranes were sprayed with a chemiluminescent reagent and exposed to film.

Primary antibodies used for Western blotting were as follows: rabbit anti–Liprin-α3-1 (1:1,000; RRID: AB_887762), rabbit anti–Liprin-α3-2 (1:200; gift from S. Schoch, Institute for Neuropathology, University of Bonn, Bonn, Germany; described in ref. 8), rabbit anti–Liprin-α3-3 (serum 4396, 1:5,000; described in ref. 9; gift from T. Südhof, Department of Molecular and Cellular Physiology and HHMI, Stanford University, Stanford, CA; RRID: AB_2617056), rabbit anti–Liprin-α1 (1:200; described in ref. 8; gift from S. Schoch), rabbit anti–Liprin-α1 (1:200; described in ref. 8; gift from S. Schoch), rabbit anti-Liprin-α2 (1:200; described in ref. 8; gift from S. Schoch); rabbit anti–Liprin-α4 (1:200; described in ref. 8; gift from S. Schoch), mouse anti-LAR (1:100; RRID: AB_10672300), mouse anti-PSD-95 (1:500; RRID: AB_10698024), mouse anti–β-actin (1:2,000; RRID: AB_476692), mouse anti–GIT-1 (1:500; RRID: AB_10672300), mouse anti-ELKS1/2α (1:1,000; RRID: AB_869944), rabbit anti-RIM1 (1:2,000; RRID: AB_2617051; gift from T. Südhof), rabbit anti-RIM1(1:1,000; RRID: AB_887774), rabbit anti–RIM-BP2 (1:500; RRID: AB_2619739), mouse anti-panMunc13 (1:100; RRID: AB_398312), rabbit anti-Munc18-1 (1:1,000; gift from T. Südhof), mouse anti-Synapsin (1:4,000; RRID: AB_2617071), rabbit anti–Synaptobrevin-2 (1:4,000; gift from T. Südhof), rabbit anti–SNAP-25 (1:2,000; gift from T. Südhof), mouse anti-Syntaxin1 (1:500; RRID: AB_528484), mouse anti-Synaptophysin (1:5,000; RRID: AB_887824), and mouse anti-Synaptotagmin1 (1:500; RRID: AB_2199314). IRDye 800CW-conjugated or IRDye 680RD-conjugated anti-mouse IgG (RRIDs: AB_621847 or AB_621848) or anti-rabbit IgG (RRID: AB_10953628 or AB_10954442) secondary antibodies were used at 1:10,000.

Immunofluorescent Staining of Cultured Neurons. DIV 14–17 neuronal cultures grown on 0.15-mm-thick chemically stripped glass coverslips were washed with PBS solution and fixed in 4% paraformaldehyde (PFA) in PBS solution at room temperature for 10 min. After three rinses in PBS solution, the neurons were blocked and permeabilized in 3% BSA/0.1% Triton X-100/PBS solution for 1 h, incubated in primary antibodies (in blocking solution) at 4 °C for 24–48 h, washed three times in PBS solution, and incubated in Oregon green 488, Alexa 555, and Alexa 633 secondary antibodies (1:200) at 4 °C for 24–48 h. Coverslips were air-dried at room temperature, mounted onto glass slides in mounting medium, and stored at 4 °C until imaging.

Primary antibodies used were as follows: monoclonal mouse anti-Bassoon^{N} (1:1,000; RRID: AB_11181058), monoclonal guinea pig anti-Bassoon^{C} (1:500; RRID: AB_2290619), rabbit anti–Liprin-α3 (serum 4396, 1:5,000; described in ref. 9; gift from T. Südhof), rabbit anti–Liprin-α2 [1:250; gift from S. Schoch (8)], anti-ELKS2α [serum E3-1029, 1:1,000; custom made (10)], rabbit anti-RIM1 (1:1,000; AB_887774), monoclonal mouse anti–PSD-95 (1:200; RRID: AB_10698024), guinea pig anti-vGlut1 (1:500; AB_887878), rabbit anti-Synapsin 1 (serum E028, 1:1,000; gift from T. Südhof), rabbit anti–RIM-BP2 (1:500; RRID: AB_2619739), and rabbit anti–Munc13-1 (1:200; RRID: AB_887735).

Confocal and STED Imaging and Analysis. Confocal and STED images were acquired with a Leica SP8 Confocal/STED 3× microscope with an oil-immersion 100×, 1.44-N.A. objective at the Harvard NeuroDiscovery Center Enhanced Imaging Core. Synapse-rich areas (23.3 × 23.3 μm^2) were selected as regions of interest (ROIs) and were scanned at a sampling frequency of ∼10 nm per pixel. Triple-color sequential confocal scans were followed by dual-color sequential STED scans by using a STED microscope with gated detectors and 40 nm *x/y* resolution and a 70-nm full width at half maximum measured with 40-nm beads. Alexa 633, Alexa Fluor 555, and Oregon green 488 were excited with 633-nm, 555-nm, and 488-nm white light lasers, respectively, at 2–5% of 1.5 mW laser power in this particular order. During STED scanning, Oregon green 488 and Alexa Fluor 555 signals were depleted with 592 nm (75% of maximum power) and 660 nm (25% of maximum power) time-gated depletion lasers. Four-times line accumulation and three-times frame averaging were applied during STED scanning. Identical settings were applied to all samples within an experiment. Images were analyzed in ImageJ with background subtraction by using a rolling ball of 0.5 μm (11). For all quantitative line-scan analyses of STED images, synapses in side view were defined as synapses that contained a synaptic vesicle cluster with an elongated Bassoon structure along the edge of the vesicle cluster. For line profile analysis, a 1-μm-long, 250-nm-wide profile was selected perpendicular to the elongated Bassoon structure across its center. An intensity profile was obtained for the synaptic vesicle cluster (imaged with confocal microscopy), the Bassoon staining (imaged by STED), and the test protein (imaged by STED). The axial position of a test protein was the *x* coordinate relative to the Bassoon maximum at which the fluorescent intensity was at maximum. A custom MATLAB program was used to analyze the distribution of the synaptic protein clusters, and all synapses were included in this analysis. In each ROI (defined as the outline of the vGluT1 vesicle cluster), Bassoon and test protein clusters (500 nm^2 < size of the detected cluster < 0.4 μm^2) were identified within the mask of the vesicle marker vGlut1. Active zone-associated components were identified as test protein clusters with ≥10% overlap with Bassoon clusters. All other synaptic protein clusters (<10% overlap with Bassoon but >10% overlap with the vesicle marker vGlut1) were classified as non–active zone-associated synaptic components. The distribution of synaptic components was calculated from individual ROIs. Protein levels in STED or confocal images were measured as the mean fluorescent intensity within an ROI. Representative images were contrast-adjusted, but all quantitative analyses were performed on original images without adjustments and were done identically for all experimental conditions. For all image acquisition and analyses comparing two or more conditions, the experimenter was blind to the condition.

Histological Analyses of Brain Sections. For histological analyses of brain sections, brains from 2–3-wk-old mice were perfusion-fixed in 0.1 M Sorensen's phosphate buffer containing 4% PFA. Cryoprotection was done in 30% sucrose overnight, and the brains were frozen in O.C.T. (Sakura Finetek) and sagittally sectioned at 40 μm in a cryostat. Brain slices mounted on glass slides were stained with 0.1% cresyl violet (Sigma Aldrich) following standard protocols, and immunostainings were performed as described for cultured cells. Slices were imaged with a slide scanner (VS120; Olympus) at the Neurobiology Imaging Facility of Harvard Medical School.

Force-Plate Analysis. Locomotor activity was assessed on two force-plate actometers (40 cm × 40 cm) as previously described (5, 12, 13). In each experiment, the center of force of a mouse was monitored for 30 min as it explored, for the first time, the open arena of the actometer in a well-lit room. Liprin-α3$^{+/+}$ and Liprin-α3$^{-/-}$ littermate mice (12 to 16 wk old) were run on the same day. The trajectory of the center of force was analyzed in three 10-min bins. The spatial confinement index and low-mobility bouts were calculated as described previously (12). Low-mobility bouts were defined as periods during which the center of force was confined to a circle of 15-mm radius for more than 10 s. For all behavioral analyses, the experimenter was blind to the genotype.

Electrophysiology. Electrophysiological recordings in cultured hippocampal neurons were performed as previously described (10). The extracellular solution contained (in mM): 140 NaCl, 5 KCl, 2 $CaCl_2$, 2 $MgCl_2$, 10 Hepes·NaOH, pH 7.4, 10 glucose (∼310 mOsm), 1 μM tetrodotoxin to block action potentials,

100 μM picrotoxin to block GABA receptors, and 50 μM D-(–)-2-Amino-5-phosphonopentanoic acid (AP5) to block NMDA receptors. All recordings were performed in whole-cell patch-clamp configuration at 20–23 °C at DIV 14–17. Whole-cell glass pipettes were pulled at 2–4 MΩ and filled with intracellular solution containing (in mM): 120 Cs-methanesulfonate, 10 EGTA, 2 $MgCl_2$, 10 Hepes·CsOH (pH 7.4), 4 Na_2-ATP, 1 Na-GTP, and 4 *N*-(2,6-dimethylphenylcarbamoylmethyl)triethylammonium chloride (~300 mOsm). Cells were held at −70 mV, and access resistance was monitored between sweeps. Cells in which access resistance exceeded 20 MΩ or in which the holding current exceeded −200 pA were excluded from the analysis. mEPSC data were acquired with an Axon 700B MultiClamp amplifier, digitized with a Digidata 1440A digitizer at 10 kHz, and analyzed by using a template search with visual inspection of each event in pClamp.

For recordings in acute hippocampal slices, 3–4-wk-old mice were deeply anesthetized by isoflurane and decapitated. Sagittal brain slices containing hippocampus (300-μm thick) were cut by using a vibratome (VT1200s; Leica) in ice-cold cutting solution containing (in mM): 75 NaCl, 2.5 KCl, 7.5 $MgSO_4$, 75 sucrose, 1 NaH_2PO_4, 12 glucose, 26.2 $NaHCO_3$, 1 Myo-inositol, 3 pyruvic acid, and 1 ascorbic acid. After cutting, slices were incubated at room temperature in incubation solution containing (in mM): 126 NaCl, 2.5 KCl, 2 $CaCl_2$, 1.3 $MgSO_4$, 1 NaH_2PO_4, 12 glucose, 26.2 $NaHCO_3$, 1 Myo-inositol, 3 pyruvic acid, and 1 ascorbic acid for at least 1 h before use. For the field recordings, slices were placed in a recording chamber continuously perfused with artificial cerebrospinal fluid (ACSF) containing (in mM): 126 NaCl, 2.5 KCl, 2 $CaCl_2$, 1.3 $MgSO_4$, 1 NaH_2PO_4, 12 glucose, and 26.2 $NaHCO_3$ at 2.5–3 mL/min (heated to 30–32 °C). All solutions were constantly bubbled with 95% O_2 and 5% CO_2. All recordings were completed within 4 h of slicing. For recording field excitatory postsynaptic potentials (EPSPs), 50 μM picrotoxin and 50 μM AP5 were added. The recording electrode was filled with ACSF with a tip resistance of 3–4 MΩ and placed ~20 μm below the slice surface in the stratum radiatum of area CA1. A concentric stimulation electrode was used for electrical stimulation and was placed 500–600 μm away from the recording site in the Schaffer collateral pathway. Bipolar stimuli (0.5 ms total) were applied to the slice every 5 s. The stimulation intensity was gradually increased from 25 to 500 μA with steps of 25 μA. Each stimulation intensity was repeated five times, and the average response was used for quantification. Data were acquired with an Axon 700B MultiClamp amplifier, digitized with a Digidata 1440A digitizer, and analyzed using pClamp.

Data acquisition and analyses for electrophysiological experiments in cultured neurons and acute slices were done by an experimenter blind to the genotype.

SypHy Imaging. SypHy and SV2-tdTomato were expressed from lentiviruses in hippocampal cultures, and cultures were imaged at DIV 14–17 and quantified as previously described (1). Briefly, experiments were performed in extracellular solution containing (in mM): 140 NaCl, 5 KCl, 2 $CaCl_2$, 2 $MgCl_2$, 10 glucose, 10 Hepes·NaOH, 0.05 AP5, and 0.025 6-cyano-7-nitroquinoxaline-2,3-dione (pH 7.4, ~310 mOsm) at 20–23 °C and imaged with an upright microscope. Images were acquired with a 60×, 1.0-N.A. water-immersion objective at 0.5 Hz with 2 × 2 binning. Neurons were stimulated at 20 Hz with a focal Nichrome bipolar electrode. NH_4Cl solution (extracellular solution substituted with NH_4Cl for 50 mM NaCl, adjusted to pH 7.4) was applied at the end of each experiment to visualize all sypHy puncta. Images were analyzed in ImageJ with background subtraction by using a rolling ball of 5 μm (11). NH_4Cl-responsive puncta for which $\%(\Delta F_{NH4Cl}/F_0) > 200\%$ were included in the analysis and were used to define ROIs. Puncta that responded to action potential stimulation [40 or 200 action potentials at 20 Hz, $\%(\Delta F_{\text{during stimulation}}/\Delta F_{NH4Cl}) > 0\%$, where $\Delta F_{\text{during stimulation}}$ is defined as the mean fluorescence of $F - F_0$ during stimulation] were defined as active synapses. SypHy F_0 was defined as the mean fluorescence during 5 s before stimulation. SypHy ΔF was quantified as fluorescence intensity F at each time point minus F_0. Peak fluorescence (ΔF_{peak}) is defined as the average ΔF during the first four imaging frames immediately following the end of the stimulation. Data were normalized to the total pool as defined by sypHy response to NH_4Cl application (ΔF_{NH4Cl}). All experiments and analyses were performed by an experimenter blind to the genotype.

Transmission EM. For glutaraldehyde fixation, DIV 14 neuronal cultures were fixed with 2% glutaraldehyde in 0.1 M sodium cacodylate buffer at 37 °C for 7.5 min, and were processed in the Conventional Electron Microscopy Facility at Harvard Medical School. Sample preparation was performed as described in ref. 1.

For high-pressure freezing, DIV-14 neuronal cultures plated on 6-mm-diameter, 0.12-mm-thick carbon-coated sapphire coverslips were transferred to extracellular solution containing (in mM) 140 NaCl, 5 KCl, 2 $CaCl_2$, 2 $MgCl_2$, 10 glucose, 10 Hepes·NaOH, pH 7.4, ~310 mOsm, and were frozen with a Leica EM ICE high-pressure freezer. Frozen samples were freeze substituted (in acetone containing 1% osmium tetroxide, 1% glutaraldehyde, and 1% H_2O), embedded in Epon, and sectioned at 50 nm by the Conventional Electron Microscopy Facility at Harvard Medical School. All samples were imaged by using a JEOL 1200EX transmission electron microscope with an AMT 2k CCD camera. All images were quantified as described in ref. 1 by using SynapseEM, a MATLAB macro provided by M. Verhage and J. Broeke, Center for Neurogenomics and Cognitive Research, Department of Functional Genomics, Vrije Universiteit Amsterdam, Amsterdam. Docked vesicles were defined as vesicles for which the vesicle membrane touches the presynaptic plasma membrane, and tethered vesicles were defined as vesicles within 100 nm of the active zone. Frequency distributions of the nearest distance of a vesicle to the plasma membrane opposed to the PSD were plotted in 10-nm bins. All experiments were performed by an experimenter blind to the genotype.

Resource Sharing and Statistics. Materials, code, and data may be shared with requesting investigators according to NIH Resource Sharing guidelines. Levels of statistical significance were set at $P \leq 0.05$, $P \leq 0.01$, and $P \leq 0.001$. Student's t tests were used for pairwise genotype comparisons of means. For multiple comparisons in rescue experiments, one-way ANOVA followed by Holm–Šídák multiple-comparisons tests were used. Two-way ANOVA followed by Holm–Šídák multiple-comparisons tests were used to compare the expression levels and localization parameters of various proteins in STED imaging, in the force plate experiments, and in the electrophysiological field recordings. The number of observations and significance values for each variable of the ANOVAs are given in the figure legend, and significance values of posttests are indicated by star symbols within the figures.

1. Wang SSH, et al. (2016) Fusion competent synaptic vesicles persist upon active zone disruption and loss of vesicle docking. *Neuron* 91:777–791.
2. Kaeser PS, et al. (2008) RIM1alpha and RIM1beta are synthesized from distinct promoters of the RIM1 gene to mediate differential but overlapping synaptic functions. *J Neurosci* 28:13435–13447.
3. Kaeser PS, et al. (2011) RIM proteins tether Ca2+ channels to presynaptic active zones via a direct PDZ-domain interaction. *Cell* 144:282–295.
4. Liu C, et al. (2014) The active zone protein family ELKS supports Ca2+ influx at nerve terminals of inhibitory hippocampal neurons. *J Neurosci* 34:12289–12303.
5. Kaeser PS, et al. (2009) ELKS2alpha/CAST deletion selectively increases neurotransmitter release at inhibitory synapses. *Neuron* 64:227–239.
6. Wang H, et al. (2013) One-step generation of mice carrying mutations in multiple genes by CRISPR/Cas-mediated genome engineering. *Cell* 153:910–918.
7. Granseth B, Odermatt B, Royle SJ, Lagnado L (2006) Clathrin-mediated endocytosis is the dominant mechanism of vesicle retrieval at hippocampal synapses. *Neuron* 51:773–786.
8. Zürner M, Mittelstaedt T, tom Dieck S, Becker A, Schoch S (2011) Analyses of the spatiotemporal expression and subcellular localization of Liprin-α proteins. *J Comp Neurol* 519:3019–3039.

9. Schoch S, et al. (2002) RIM1alpha forms a protein scaffold for regulating neurotransmitter release at the active zone. *Nature* 415:321–326.
10. Held RG, Liu C, Kaeser PS (2016) ELKS controls the pool of readily releasable vesicles at excitatory synapses through its N-terminal coiled-coil domains. *eLife* 5:e14862.
11. Sternberg SR (1983) Biomedical image processing. *Computer (Long Beach Calif)* 16: 22–34.
12. Fowler SC, Birkestrand B, Chen R, Vorontsova E, Zarcone T (2003) Behavioral sensitization to amphetamine in rats: Changes in the rhythm of head movements during focused stereotypies. *Psychopharmacology (Berl)* 170:167–177.
13. Fowler SC, et al. (2001) A force-plate actometer for quantitating rodent behaviors: Illustrative data on locomotion, rotation, spatial patterning, stereotypies, and tremor. *J Neurosci Methods* 107:107–124.

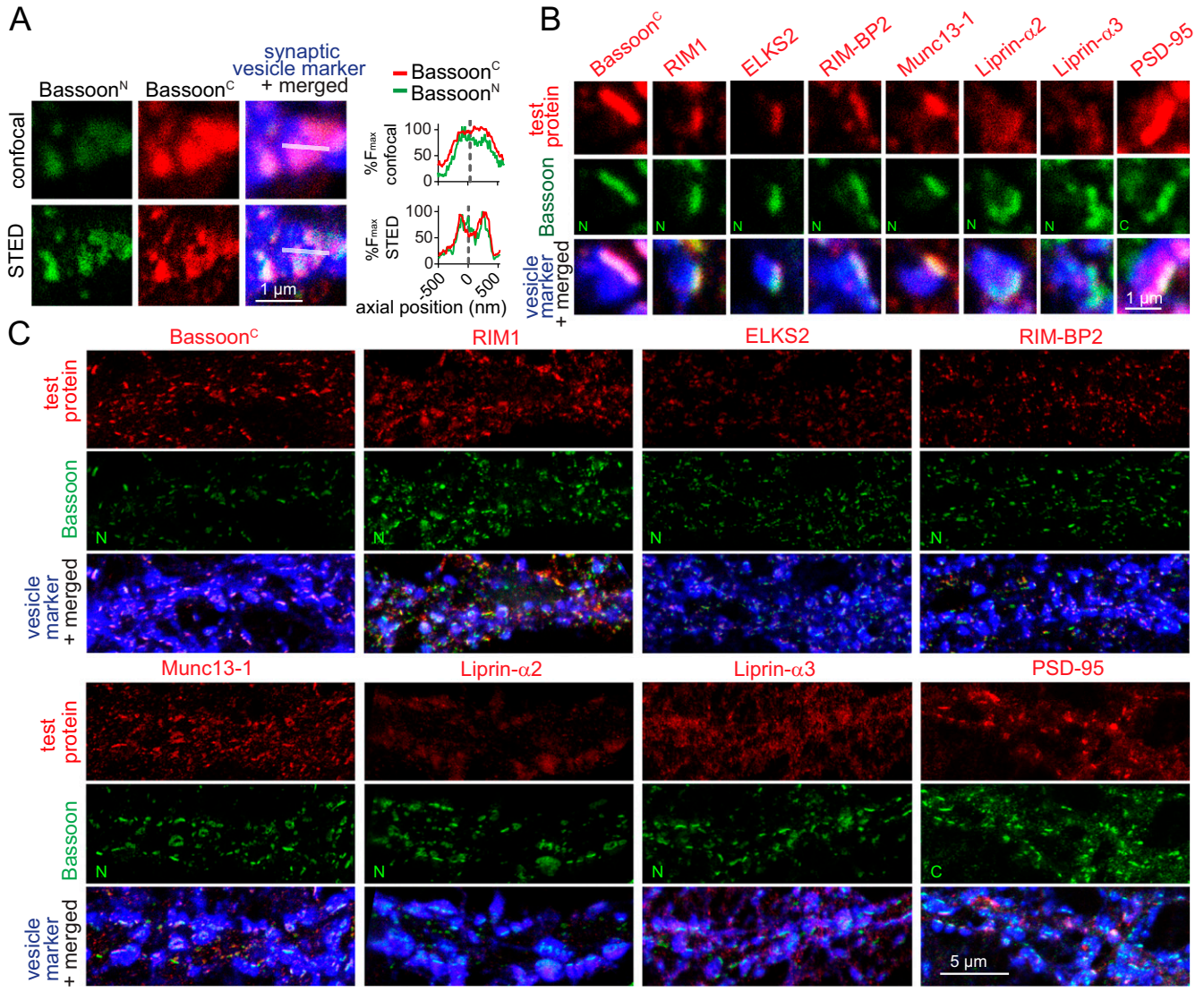

Fig. S1. Synapse in face view and additional images for Fig. 1. (*A*) Example images and line scans of a synapse stained for Bassoon^N and Bassoon^C in face view. Confocal scanning shows disk-like Bassoon structures, whereas STED images of the same synapse resolve a distinct doughnut-shaped structure of the Bassoon cluster. Synapsin was used as a marker to label the boundary of presynaptic boutons and was imaged by confocal microscopy. (*B*) Confocal scans of the STED images shown in Fig. 1*C*. (*C*) Overview STED images of cultured hippocampal neurons shown in Fig. 1.

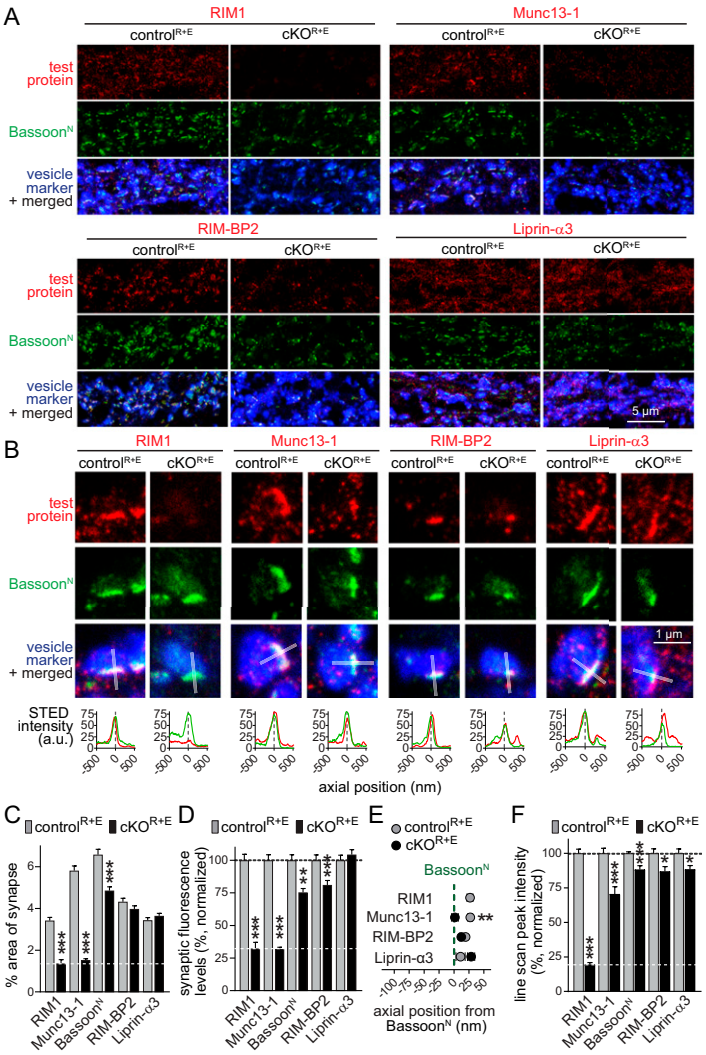

Fig. S2. Liprin-α3 localization at cKO^{R+E} synapses. (*A*) Representative overview STED images of various test proteins in control^{R+E} and cKO^{R+E} synapses (1). For generation of cKO^{R+E} synapses, neurons with floxed alleles for RIM1, RIM2, ELKS1α, and ELKS2α were infected with lentiviruses expressing cre recombinase (cKO^{R+E}) and inactive control viruses (control^{R+E}). We have previously established that this leads to strongly disrupted active zones, with almost complete loss of Munc13, ∼80% loss of Bassoon, ∼60% loss of Piccolo, and ∼50% loss of RIM-BP2 as assessed by Western blotting and confocal microscopy (1). *vGlut1* antibodies were used to label excitatory nerve terminals imaged simultaneously with confocal microscopy. (*B*) Representative side-view STED images and line profiles [as in Fig. 1, but showing arbitrary units (a.u.)] of various test proteins in control and cKO^{R+E} synapses. Dashed line at zero indicates the localization of the Bassoon^{N} peak. (*C*) Analysis of the percentage area covered by test proteins within synapses as defined by the vesicular marker vGlut1. All analyses presented here are biased toward synapses with more Bassoon because Bassoon is required for identification of side-view synapses and active-zone–like structures, but many cKO^{R+E} synapses have little Bassoon (1). Dashed white line indicates the noise level as assessed by RIM1 staining: RIM1 (control^{R+E}, $n = 462$ synapses/3 cultures; cKO^{R+E}, $n = 465/3$); Munc-13–1 (control^{R+E}, $n = 750/3$; cKO^{R+E}, $n = 607/3$); RIM-BP2 (control^{R+E}, $n = 617/3$; cKO^{R+E}, $n = 792/3$); Bassoon (control^{R+E}, $n = 519/3$; cKO^{R+E}, $n = 724/3$); and Liprin-α3 (control^{R+E}, $n = 519/3$; cKO^{R+E}, $n = 724/3$). Statistical significance was determined by two-way ANOVA (genotype, test protein, and interaction significant at $P \leq 0.001$) followed by Holm–Šídák posttests (reported in figure) for multiple comparisons. (*D*) Analysis of synaptic fluorescence levels integrated over the area labeled by the excitatory synaptic vesicle marker vGlut1, expressed normalized to the average of control^{R+E} values (dashed black line). Dashed white line indicates the noise level as assessed by RIM1 staining. Numbers of synapses/cultures are as in *C*. The reduction in Bassoon staining is somewhat milder than that observed previously (1), which is likely the result of a selection bias because here we select for synapses that contain Bassoon, and may also be influenced by the differences between STED and confocal microscopy, e.g., nonlinearities associated with STED imaging. Statistical significance was determined by two-way ANOVA (genotype, test protein, and interaction significant at $P \leq 0.001$) followed by Holm–Šídák posttests (reported in figure) for multiple comparisons. (*E*) Axial positions of the test proteins relative to Bassoon^{N} (dashed line) determined by the peak localization in intensity profiles of individual images of synapses in side view. Negative values are proximal of Bassoon^{N} inside the nerve terminal, and positive values are distal toward the postsynaptic compartment: RIM1 (control^{R+E}, $n = 83/3$); Munc13-1 (control^{R+E}, $n = 86/3$; cKO^{R+E}, $n = 77/3$); RIM-BP2 (control^{R+E}, $n = 86/3$; cKO^{R+E}, $n = 92/3$); and Liprin-α3 (control^{R+E}, $n = 88/3$; cKO^{R+E}, $n = 108/3$). RIM1 peak localization for cKO^{R+E} is not shown because it is by definition artifactual as a result of absence of the antigen. Statistical significance determined by two-way ANOVA (genotype significant at $P \leq 0.001$; test protein significant at $P \leq 0.01$; interaction significant at $P \leq 0.001$) followed by Holm–Šídák multiple-comparisons posttests (reported in figure) for peak localization of each test protein in cKO^{R+E} neurons to control^{R+E} neurons. (*F*) Peak intensity of cKO^{R+E} line scans normalized to control^{R+E} (dashed black line). Dashed white line indicates the noise level as assessed by RIM1 staining: RIM1 (control^{R+E}, $n = 83/3$; cKO^{R+E}, $n = 57/3$); Munc13-1 (control^{R+E}, $n = 86/3$; cKO^{R+E}, $n = 77/3$); Bassoon^{N} (control^{R+E}, $n = 343/12$; cKO^{R+E}, $n = 334/12$); RIM-BP2 (control^{R+E}, $n = 86/3$; cKO^{R+E}, $n = 92/3$); and Liprin-α3 (control^{R+E}, $n = 88/3$; cKO^{R+E}, $n = 108/3$). Statistical significance determined by two-way ANOVA (genotype, test protein, and interaction significant at $P \leq 0.001$) followed by Holm–Šídák multiple-comparisons posttests (reported in figure) for comparing peak intensity of each protein in cKO^{R+E} neurons to control^{R+E} neurons. All data are means ± SEM (*$P \leq 0.05$, **$P \leq 0.01$, and ***$P \leq 0.001$). Although these data indicate that Liprin-α3 localization is not strongly impaired upon KO of RIM and ELKS, it is possible that mild impairments exist but are not detected as a result of a selection bias by only including Bassoon-positive cKO^{R+E} synapses.

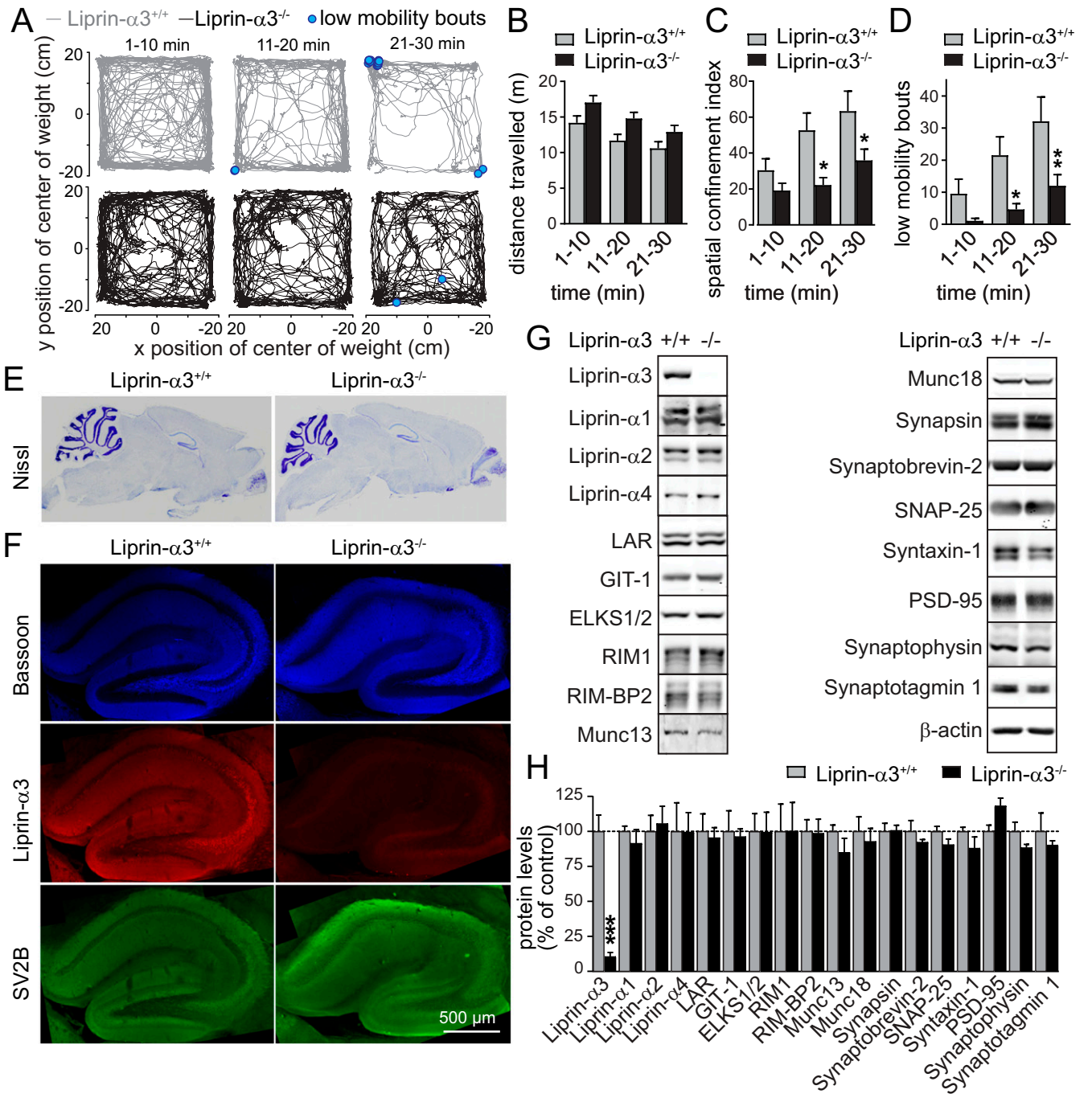

Fig. S3. Analysis of locomotion and hippocampal morphology and protein composition in Liprin-α3$^{-/-}$ mice. (*A*) Representative trajectories of a Liprin-α$^{-/-}$ mouse and a Liprin-α3$^{+/+}$ littermate control mouse from a continuous single trial recording of 30 min of open-field behavior in a 40-cm × 40-cm force-plate actometer, separated in three 10-min bins. Blue circles indicate low-mobility bouts. (*B–D*) Quantitative analysis of the distance traveled (*B*), the spatial confinement (*C*), and the number of low-mobility bouts (*D*) in trajectories (n = 9 littermate pairs). Statistical significance determined by two-way ANOVA (*B*, genotype significant at $P \leq 0.05$; time significant at $P < 0.001$; interaction n.s.; *C*, genotype significant at $P \leq 0.05$; time significant at $P < 0.001$; interaction significant at $P \leq 0.05$; *D*, genotype significant at $P \leq 0.05$; time significant at $P < 0.001$; interaction n.s.) followed by Holm–Šídák multiple-comparisons posttests (reported in figures). (*E*) Images of sagittal brain sections of 3-wk-old littermate Liprin-α3$^{+/+}$ and Liprin-α3$^{-/-}$ mice labeled by Nissl staining. (*F*) Images of hippocampi in sagittal brain sections of 3-wk-old littermate Liprin-α3$^{+/+}$ and Liprin-α3$^{-/-}$ mice labeled for Bassoon^{N}, Liprin-α3, and the synaptic vesicle protein SV2B. Note that all immunostainings were done with the Liprin-α3 antibody 3, which mildly cross-reacts with other Liprin-α proteins in Western blotting, but shows a strong decrease in immunostaining. (*G*) Representative Western blots using fluorescent secondary antibodies of homogenates from the hippocampi of a Liprin-α3$^{-/-}$ mouse and a Liprin-α3$^{+/+}$ littermate control mouse. (*H*) Quantification of fluorescent signals shown in *G*. All fluorescent signals were normalized to a β-actin loading control run in the same lane and expressed normalized to the average of Liprin-α3$^{+/+}$ mice (dashed black line; n = 3 littermate pairs). All data are means ± SEM [*$P \leq 0.05$, **$P \leq 0.01$, and ***$P < 0.001$; n.s., not significant; two-way ANOVA followed by Holm–Šídák multiple-comparisons posttests (*B–D*) or by Student's t test (*H*)].

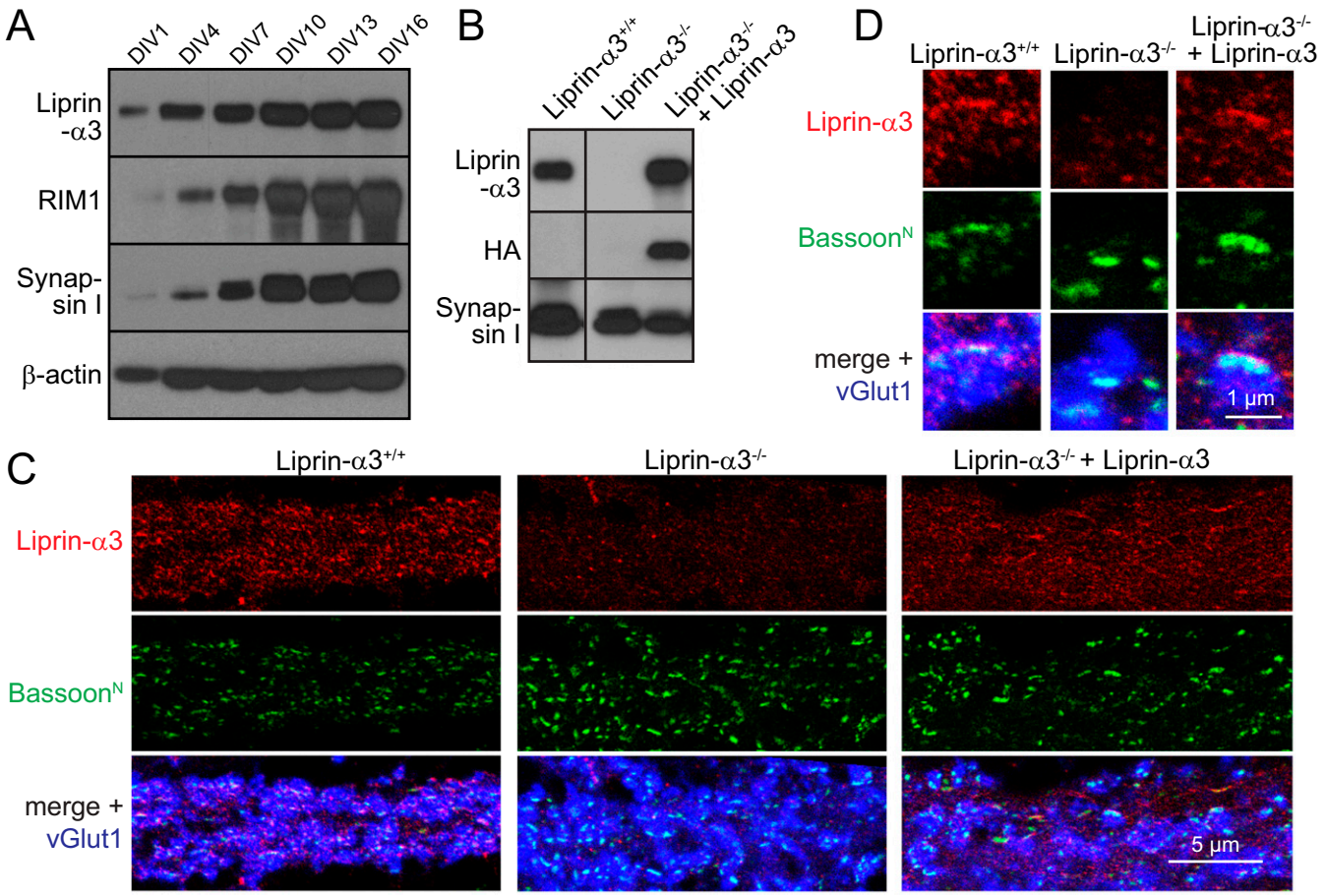

Fig. S4. Expression and localization of rescue Liprin-α3 upon lentiviral transduction at DIV 1. (*A*) Time course of expression of Liprin-α3, RIM1, and Synapsin I in cultured hippocampal neurons harvested at indicated DIVs. (*B*) Liprin-α3$^{+/+}$ neurons, Liprin-α3$^{-/-}$ neurons, and Liprin-α3$^{-/-}$ neurons rescued with lentiviral expression of Liprin-α3 were used for imaging of synaptic vesicle exocytosis. Western blots show Liprin-α3 expression in Liprin-α3$^{+/+}$ neurons, Liprin-α3$^{-/-}$ neurons, and Liprin-α3$^{-/-}$ neurons transduced with lentiviral rescue Liprin-α3 (human synapsin promoter driven, HA-tagged) at DIV 1. Neurons were harvested for Western blotting at DIV 14. All bands for a given antibody are from the same blot displayed with identical contrast and intensity settings. Images were cropped to remove additional irrelevant lanes. (*C* and *D*) Representative STED images of hippocampal neurons immunostained with Liprin-α3 and Bassoon^{N} antibodies showing localization of rescue Liprin-α3 within nerve terminals in overview images (*C*) and at high magnification (*D*). vGlut1 antibodies were used to label the synaptic vesicle cluster and the vGlut1 signal was imaged with confocal microscopy.

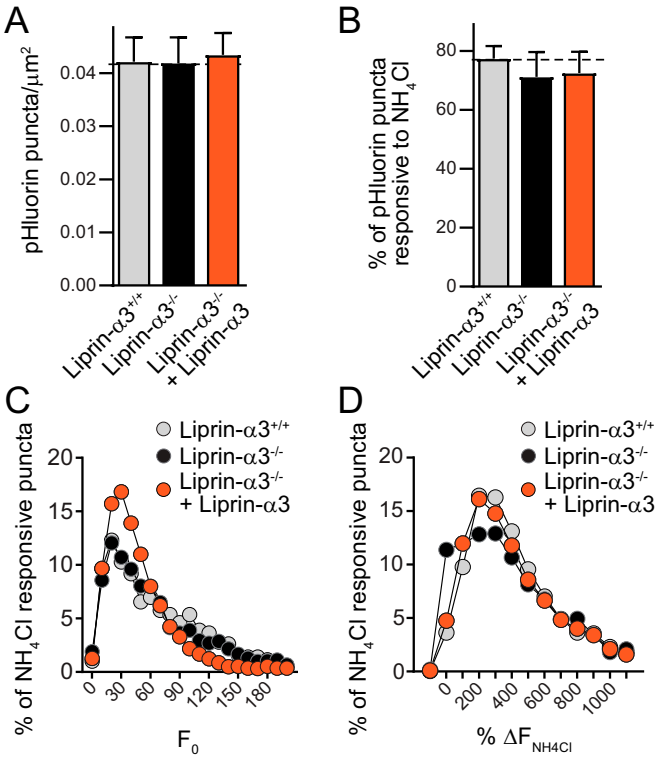

Fig. S5. Additional analyses of sypHy imaging data. (*A*) Average sypHy puncta density in cultured Liprin-α3$^{+/+}$ neurons, Liprin-α3$^{-/-}$ neurons, and Liprin-α3$^{-/-}$ neurons rescued with lentiviral expression of Liprin-α3. Numbers of synapses/cultures are as in Fig. 3. (*B*) Percentage of sypHy puncta responsive to NH_4Cl. Numbers of synapses/cultures are as in Fig. 3. (*C* and *D*) Frequency distributions of fluorescent signal of sypHy puncta at baseline (*C*; F_0 before stimulation) and upon NH_4Cl application (*D*). Numbers of synapses/cultures are as in Fig. 3 *C*–*J*.

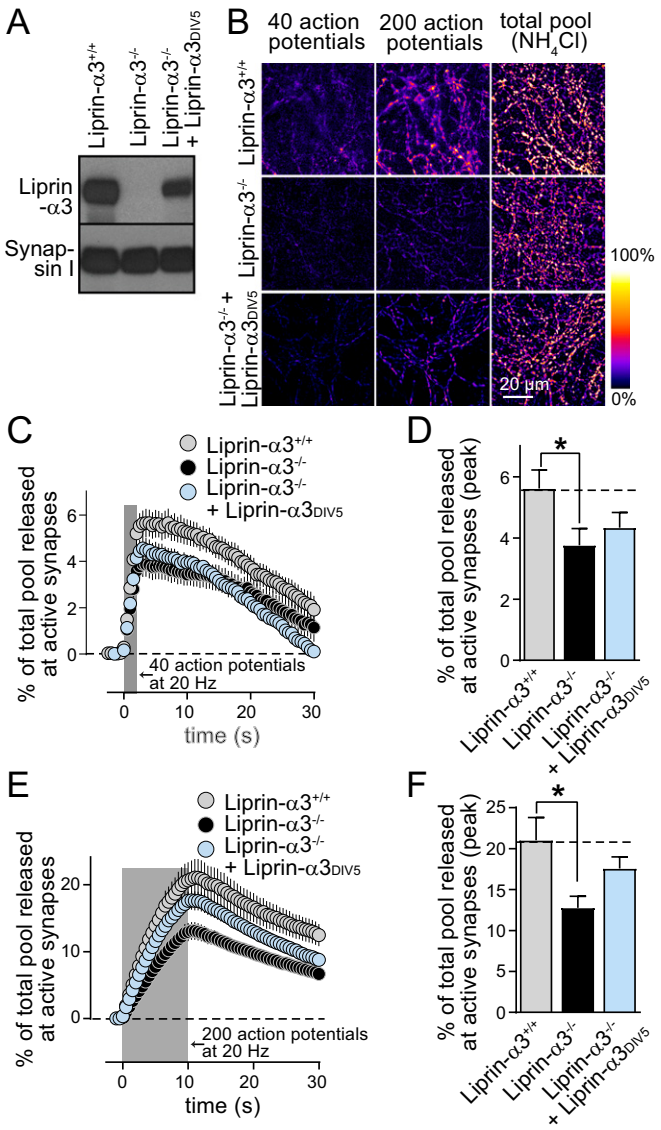

Fig. S6. DIV-5 transduction with Liprin-α3 rescue viruses impairs expression and rescue. Liprin-α3$^{+/+}$ neurons, Liprin-α3$^{-/-}$ neurons, and Liprin-α3$^{-/-}$ neurons expressing Liprin-α3 from a lentivirus were used for imaging of synaptic vesicle exocytosis. In the experiment shown in this figure, Liprin-α3$^{-/-}$ neurons were transduced with lentiviral Liprin-α3 (human synapsin promoter driven, HA-tagged) at DIV 5 (Liprin-α3$^{-/-}$ + Liprin-α3$_{DIV5}$). (*A*) Representative Western blot of expression of Liprin-α3. Note that the lentiviral rescue Liprin-α3 expression level appears lower than in neurons transduced with the same virus at DIV 1 (Fig. S4*B*). (*B*) Pseudocolored images of sypHy-expressing Liprin-α3$^{+/+}$ and Liprin-α3$^{-/-}$ neurons, and Liprin-α3$^{-/-}$ neurons rescued with lentiviral expression of Liprin-α3 at DIV 5. Neurons were stimulated with 40 or 200 action potentials and dequenched with NH_4Cl. Images represent peak fluorescence change. (*C* and *D*) Quantification of fluorescence changes in active synapses of neurons stimulated with 40 action potentials at 20 Hz (*C*, gray area) showing the time course of the mean fluorescence change in active synapses as a percentage of the fluorescence increase upon NH_4Cl application (*C*) and the peak response of active synapses (*D*). Liprin-α3$^{+/+}$, n = 1,585 NH_4Cl-responsive synapses/1,071 active synapses/9 coverslips/3 independent cultures; Liprin-α3$^{-/-}$, 1583/954/9/3; Liprin-α3$^{-/-}$ + Liprin-α3$_{DIV5}$, n = 1,709/977/9/3. (*E* and *F*) Quantification as in *C* and *D* but for neurons stimulated with 200 action potentials. Liprin-α3$^{+/+}$, n = 1,585/1,117/9/3; Liprin-α3$^{-/-}$, 1,583/1,173/9/3; Liprin-α3$^{-/-}$ + Liprin-α3, n = 1,709/1,282/9/3. All data are means ± SEM (*$P \leq 0.05$, one-way ANOVA followed by Holm–Šídák multiple-comparisons test comparing each condition vs. Liprin-α3$^{-/-}$). The number of coverslips was used as a basis for statistics in pHluorin imaging experiments. This experiment reveals that only DIV-1 transduction with lentiviruses expressing Liprin-α3 (Fig. 3 and Fig. S4) is sufficient to fully restore Liprin-α3 expression and to provide significant rescue in Liprin-α3$^{-/-}$ neurons, whereas later transduction leads to lower expression and inefficient rescue.

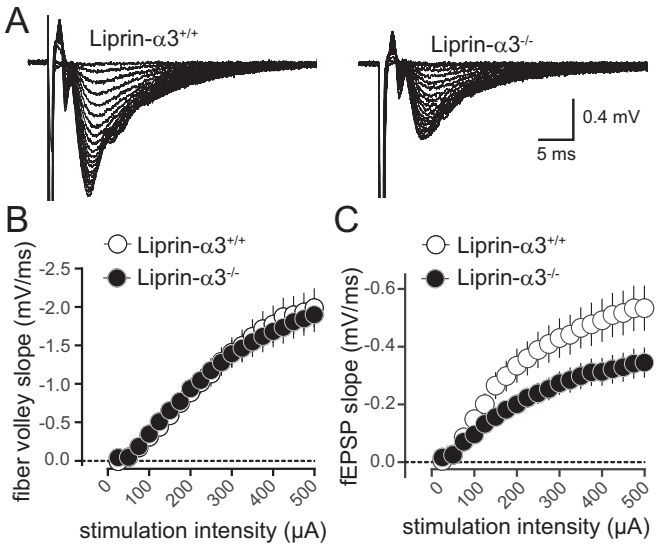

Fig. S7. Analyses of synaptic transmission in brain slices of Liprin-α3–KO mice. (*A*) Example traces of field ESPS (fEPSP) recordings in stratum radiatum of area CA1 in acute slices of the hippocampus in Liprin-$\alpha3^{+/+}$ and Liprin-$\alpha3^{-/-}$ littermate mice. Schaffer collaterals were stimulated with a concentric stimulation electrode at increasing stimulation intensities. (*B* and *C*) Quantification of the fiber volley slope (*B*) and the fEPSP slope (*C*) as a function of stimulation intensity for the experiment shown in *A* (Liprin-$\alpha3^{+/+}$, $n = 25$ slices/7 mice; and Liprin-$\alpha3^{-/-}$, $n = 29/7$). Statistical significance determined by two-way ANOVA [*B*, genotype not significant (n.s.), intensity significant at $P \leq 0.001$, interaction n.s.; *C*, genotype significant at $P \leq 0.001$, intensity significant at $P \leq 0.001$, interaction n.s.]. All data are means ± SEM.

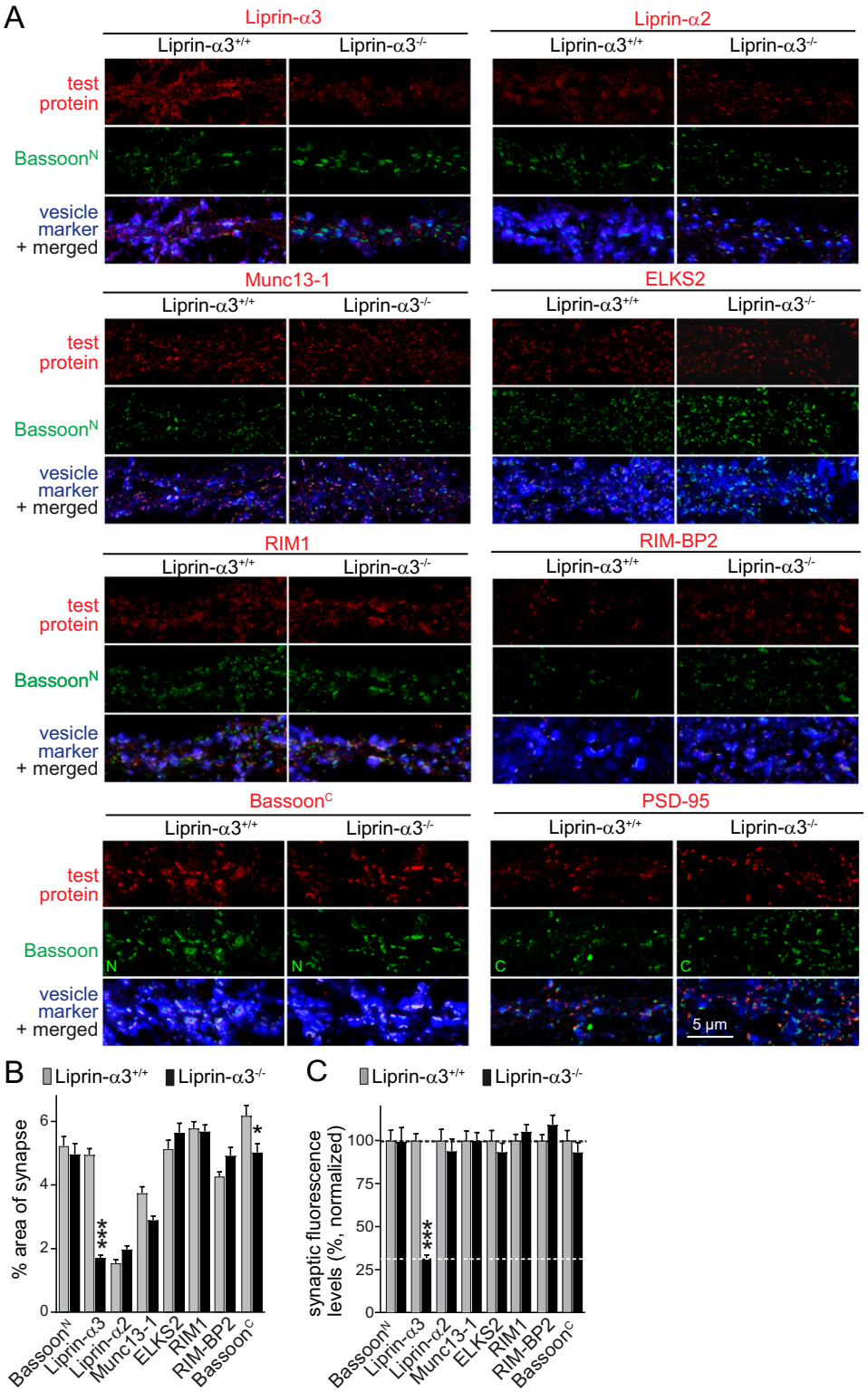

Fig. S8. Additional STED microscopy data related to Fig. 5. (*A*) Overview STED images of the experiment shown in Fig. 5. (*B*) Analysis of the percentage of the area covered by test proteins within synapses as defined by the vesicular marker vGlut1: Bassoon^{N} ($^{+/+}$, $n = 533$ synapses/3 cultures; $^{-/-}$, $n = 332/3$); Liprin-α3 ($^{+/+}$, $n = 485/3$; $^{-/-}$, $n = 550/3$); Liprin-α2 ($^{+/+}$, $n = 546/3$; $^{-/-}$, $n = 729/3$); Munc13-1 ($^{+/+}$, $n = 599/3$; $^{-/-}$, $n = 666/3$); ELKS2 ($^{+/+}$, $n = 697/3$; $^{-/-}$, $n = 589/3$); RIM1 ($^{+/+}$, $n = 642/3$; $^{-/-}$; $n = 360/3$); RIM-BP2 ($^{+/+}$, $n = 744/3$; $^{-/-}$, $n = 730/3$); and Bassoon^{C} ($^{+/+}$, $n = 533/3$; $^{-/-}$, $n = 332/3$). Statistical significance was determined by two-way ANOVA (genotype, test protein, and interaction significant at $P \leq 0.001$) followed by Holm–Šídák posttests for multiple comparisons (reported in figure). (*C*) Analysis of fluorescence levels integrated over the synapse area normalized to the average of Liprin-α3$^{+/+}$ synapses. Numbers of synapses/cultures are as in *B*. Statistical significance was determined by two-way ANOVA (genotype significant at $P \leq 0.01$, test protein significant at $P \leq 0.001$, interaction significant at $P \leq 0.001$) followed by Holm–Šídák posttests for multiple comparisons (reported in figure). All data are means ± SEM (*$P \leq 0.05$ and ***$P \leq 0.001$).

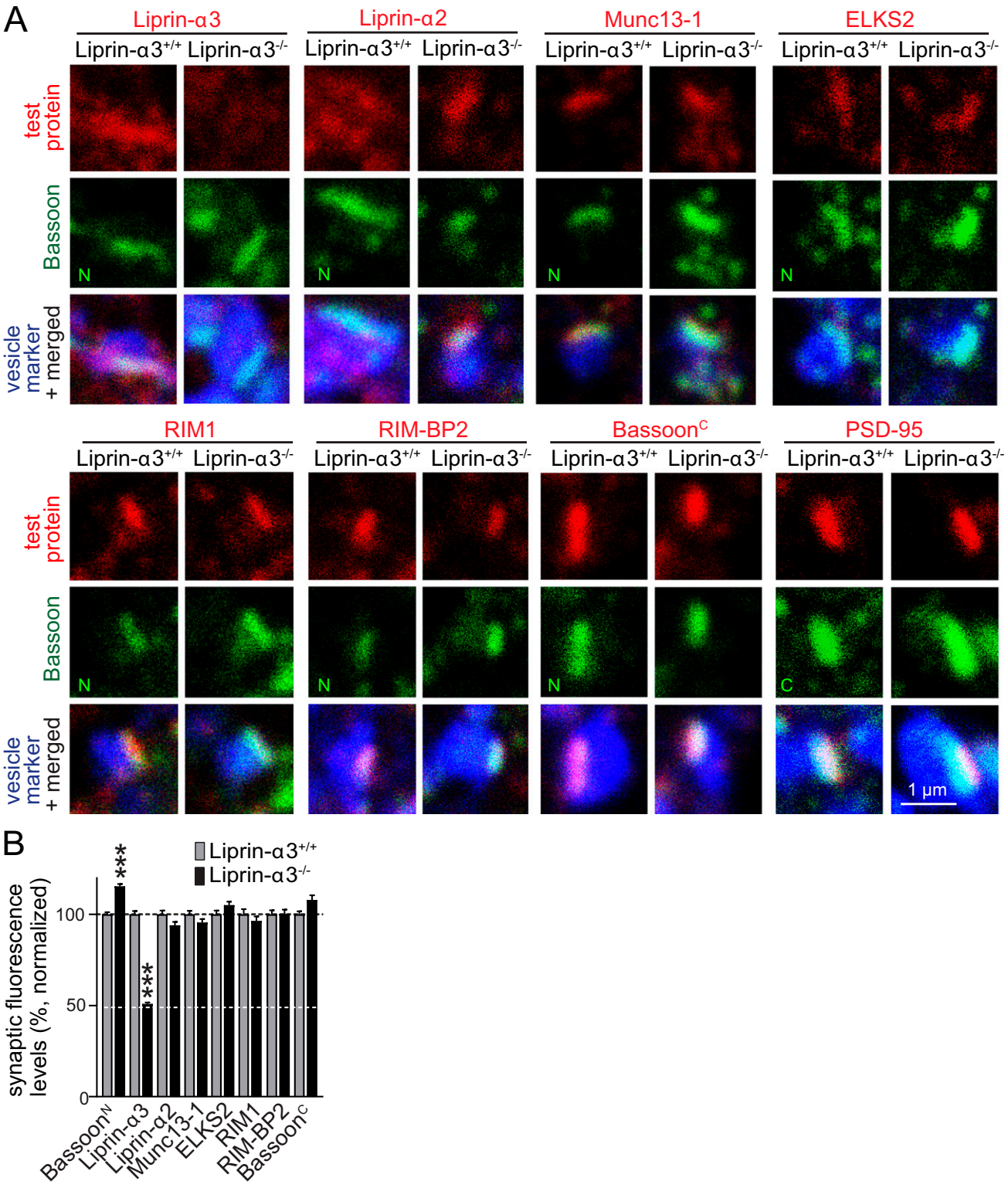

Fig. S9. Analysis of synaptic protein levels in confocal images of Liprin-α3$^{-/-}$ synapses. Nonlinearities in the signal intensity may affect protein level measurements in STED images. To circumvent this limitation, we analyzed confocal scans of the experiment shown in Fig. 5 to assess synaptic fluorescence levels. (*A*) Confocal images of the same synapses that are shown in Fig. 5*A*. (*B*) Analyses of synaptic fluorescence in confocal images, plotted as the mean fluorescence levels within the synapse area defined by the vesicle marker normalized to the average of Liprin-α3$^{+/+}$ synapses: Bassoon^{N} ($^{+/+}$, n = 3,150 synapses/8 cultures; $^{-/-}$, n = 3,330/8); Liprin-α3 ($^{+/+}$, n = 973/3; $^{-/-}$, n = 550/3); Liprin-α2 ($^{+/+}$, n = 472/3; $^{-/-}$, n = 410/3); Munc-13 ($^{+/+}$, n = 599/3; $^{-/-}$, n = 556/3); ELKS2 ($^{+/+}$, n = 559/3; $^{-/-}$, n = 605/3); RIM1 ($^{+/+}$, n =517/3; $^{-/-}$, n = 360/3); RIM-BP2 ($^{+/+}$, n = 394/3; $^{-/-}$, n = 499/3); and Bassoon^{c} ($^{+/+}$, n = 533/3; $^{-/-}$, n = 425/3). Statistical significance was determined by two-way ANOVA (genotype, test protein, and interaction significant at $P \leq 0.001$) followed by Holm–Šídák posttests for multiple comparisons (reported in figure).